Simultaneous Electrical, Electrochemical, and Optical Relaxation Measurements of Oxygen Surface Exchange Coefficients: $Sr(Ti,Fe)O_{3-d}$ Film Crystallization Case Study

Emily J. Skiba[1, ‡], Ting Chen[2, †, ‡], and Nicola H. Perry[1,2]*

[1] Department of Materials Science & Engineering and Materials Research Laboratory, University of Illinois at Urbana-Champaign, 1304 W Green St, Urbana IL 61801, U.S.A.

[2] International Institute for Carbon-Neutral Energy Research, Kyushu University, 744 Motooka, Nishi-ku Fukuoka, 819-0395 Japan

KEYWORDS

Perovskite. Crystallization. Impedance spectroscopy. Electrical Conductivity Relaxation. Optical Transmission Relaxation.

ABSTRACT

The oxygen surface exchange coefficient (k) dictates efficiency and response time of many mixed conductors, so its accurate, continuous measurement in realistic conditions, enabling rational tailoring, is necessary. However, recent results showed that k values determined by a thin film optical transmission relaxation (OTR) method were orders of magnitude lower than those extracted from the cross-cell AC-impedance spectroscopy (AC-IS) approach, and similar discrepancies among methods exist in the literature. OTR has also detected dramatic increases in k in situ during crystallization. Therefore, in this work, we sought to establish whether k values from OTR are reliable, and to gain further insight into crystallization-induced changes, via comparison to the electrical conductivity relaxation (ECR) method. We performed simultaneous OTR and ECR measurements on the same region of an as-grown amorphous $SrTi_{0.65}Fe_{0.35}O_{2.825+\delta}$ (STF) film, prepared by pulsed laser deposition and characterized by Rutherford Backscattering Spectroscopy, during thermal treatment to induce crystallization and a large increase in k. We also compared cross-cell AC-IS vs. OTR on an as-grown amorphous film during crystallization and OTR vs. ECR on a crystalline-grown film. Simultaneous measurements eliminate variability in k between samples or due to different thermal/gas history. OTR and ECR methods yielded the same k values, and the same crystallization temperature, within error. Both isothermal optical absorption and electrical conductivity changes are proportional to the hole and oxygen concentration changes under the conditions of this study. However, while OTR was able to measure optical absorption changes under all the conditions tested, ECR was not viable in the high resistance regime. Cross-cell AC-IS k values were elevated vs. OTR values, were less stable over time, and were only accessible in limited conditions. We discuss the potential impacts of current collectors and oxygen exchange driving force on k values determined by cross-cell AC-IS vs. ECR vs. OTR.

1. Introduction

Mixed ionic and electronic conducting (MIEC) oxides, such as the cubic perovskite $SrTi_{1-x}Fe_xO_{3-x/2+\delta}$ (STF), play a vital role in gas separation membranes [1–4], gas sensors [5,6], and solid oxide fuel/electrolysis cells (SOFCs/SOECs)[7–11]. They are chosen for their ability to conduct both mobile oxygen vacancies and electronic carriers, which results in higher oxygen surface exchange coefficients (k) than pure electronic conductors, as the full surface may participate in the reaction.[4] These surface exchange coefficients, representing the proportionality between the oxygen flux across the surface and the electrochemical potential gradient driving force[12], often dictate efficiency of MIEC components in the aforementioned applications. For example, sluggish oxygen surface exchange kinetics can lead to large polarization losses at the cathode of SOFCs or anode of SOECs [9,13,14]. Owing to the relatively high activation energy of the oxygen exchange process, as operating temperatures are reduced into the intermediate range (400-600 ˚C) for durability and cost benefits[7–9], these losses become particularly deleterious, limiting the overall device performance. Further, the k values are dynamic and sensitive to changes in surface chemistry [15,16], microstructure [17–19], orientation [20], and crystallinity [21], as may be brought about by processing or operating conditions. In order to better understand oxygen exchange behavior, precise and accurate, continuous characterization of the oxygen surface exchange coefficient of native surfaces in realistic operating conditions is necessary.

Various techniques exist for the analysis of oxygen diffusivity (D) and chemical (k_{chem}), electrical (k_q), or tracer (k*) surface exchange coefficients, namely: cross-cell ac impedance spectroscopy (AC-IS),[22–26] isotope exchange depth profiling (IEDP),[27,28] wafer curvature relaxation[29], lattice parameter relaxation,[30] electrical conductivity relaxation (ECR),[31–34] and optical transmission relaxation (OTR)[18,21,24,26,35,36]. Each of these techniques has advantages and

disadvantages, in the context of determination of mass transport kinetics in MIECs, summarized in Table 1.

Table 1: *Summary of methods for measuring surface exchange coefficients.*

Technique	Continuous?	Native Surface?	Notes
IEDP (k*)	×	~	Requires highly dense samples [37]
			Insulators may require O introduction through labeled H2O or catalytic coatings
			Improper quenching may lead to misinterpretation of data from grain boundary tailing
			Challenging sample preparation: surface polishing and cleaning[38]
Cross-cell AC-IS (k_q, k_{chem})	✓	×	Requires porous current collectors on entire MIEC surface
			Challenging data interpretation due to multiple, sometimes overlapping, features[39]
Curvature relaxation (k_{chem})	✓	✓	Requires chemo-mechanically active sample with linear elasticity
			Assumes constant elastic modulus with pO_2 change
Lattice relaxation (k_{chem})	✓	✓	Requires chemo-mechanically active sample with linear chemical expansion behavior
ECR (k_{chem})	✓	?	Unknown contribution to k_{chem} from current collectors adjacent to native surface under test
			Assumes constant carrier mobility with pO_2 change
OTR (k_{chem})	✓	✓	Requires optically active sample
			Assumes constant extinction coefficient with pO_2 change

As there are several techniques for measurement of k in MIECs, it is important to understand whether each technique would be able to reproduce the results of the others if conducted on the same sample at the same time. Reference 40 compiled oxygen surface exchange coefficient values for several of the commonly studied mixed conducting oxides of the (La,Sr)(Co,Fe,Ti)$O_{3-\delta}$ family. Comparisons of oxygen surface exchange coefficients in $SrTi_{1-x}Fe_xO_{3-x/2+\delta}$(STF), (La,Sr)(Co,Fe)$O_{3-\delta}$ (LSCF), and (La,Sr)$FeO_{3-\delta}$ (LSF) showed orders of magnitude variations between ECR, cross-cell AC-IS, and IEDP derived k values for the same composition, although LSC appeared to have relatively consistent k values across several techniques. Work on the primarily electronic conducting system (La,Sr)$MnO_{3-\delta}$ (LSM) shows similar disagreements in the literature. LSM k* values determined by Navickas et al.[17] and De Souza et al., [28] both using IEDP, differ by 2-3 orders of magnitude, possibly due to different thermal histories of the films vs. bulk ceramics, respectively. (The grain boundary density also varied, but the grain k* value of the films, not the grain boundary k*, was compared to the bulk ceramic k*). Using ECR on LSM thin films, Yan et al. [19] investigated the relative contribution of the grains' surface and of grain boundaries intersecting the surface on k_{chem}. Although the k_{chem} values agreed with several others in the literature [28,41–43] there was poor agreement with the equivalent k_{chem} values converted from cross-cell AC-IS data in Fleig et al.'s[44] work on 250 nm LSM microelectrodes at 800°C. However, for such *non-simultaneous* comparisons on different samples, it is difficult to be certain whether discrepancies in k values truly arise from the techniques themselves or from actual differences in k values resulting from inter-sample variations or thermal history differences.

Further complications may stem from quantifying error bars or uncertainty related to geometry or morphology effects. As noted by Armstrong et al.,[45] several of the k values present in the literature were extracted from samples with thicknesses approaching or greater than the critical

length (L_c = D/k), without sensitivity analysis to estimate error bars on k extracted in the mixed (both k- and D-limited) kinetic regime. Similarly, comparing the k_{chem} values extracted from porous and dense samples of $La_{0.6}Sr_{0.4}CoO_{3-\delta}$, Ganeshananthan et al.[46] saw a large discrepancy in the temperature dependence of k_{chem} values, attributed to the temperature dependence of surface adsorbate coverage for the porous samples vs. the possible rate-limiting role of bulk diffusivity in the dense samples limiting accuracy of the extracted k_{chem} values. Generally, studies on porous MIEC electrodes suffer from the disadvantage of stochastic microstructure and an ill-defined active region geometry. While tomographic reconstructions can aid analysis[47], it remains very difficult to separate fully the influence of the electrode morphology from "intrinsic" properties of the material and thus to get comparable quantitative data for different compositions.

Based on these discrepancies, there is a clear need for direct, *simultaneous* comparisons of techniques on the same sample, to deconvolute the contributions of sample variations vs. technique effects to derived k values. To date, only very limited simultaneous studies have been conducted, such as OTR vs. cross-cell AC-IS. Notably, Kim et al. performed a comparison of cross-cell AC-IS derived k_q and OTR derived k_{chem} for crystalline 10 mol% Pr-doped CeO_2 (PCO) films. [48,49] Results showed that the impedance-derived k values were up to two orders of magnitude higher than the optical k values, possibly due to the presence of Pt current collectors needed for the cross-cell AC-IS measurements. Similarly, our previous work conducted on the crystalline STF system has shown a large disagreement between values of k extracted from cross-cell AC-IS vs. OTR.[24] Optically measured k_{chem} values were orders of magnitude lower than the impedance derived k_{chem} values and k_q values normalized by the thermodynamic factor, thus suggesting that both the sputtered porous Pt and painted porous Au current collectors used for the cross-cell AC-IS measurements may have contributed to enhancing the resulting k_{chem} and k_q values.

Given the disagreement, in order to have confidence in the k_{chem} values extracted from OTR measurements specifically, we need to observe agreement with k_{chem} values determined from other techniques, for the exact same sample and measurement conditions. Consequently, it was the goal of this work to measure k_{chem} by both ECR and OTR simultaneously in order to verify the applicability and accuracy of the OTR technique for the STF material system and thus support the broader application of this technique to other material systems. To achieve this goal, two key stipulations were upheld to ensure the validity and accuracy of technique comparisons in this work: 1) The measurements must be conducted on the same sample to ensure that there exist no differences in processing conditions that could alter point defect concentrations, surface chemistry, or microstructure; 2) The two types of measurements must occur at the same time to remove any extraneous variables introduced by differences in environment or thermal history, which may lead to alterations to the surface chemistry and properties of the material.

Further, in light of our previous work illustrating the superior oxygen exchange kinetics of as-grown amorphous STF35 films upon subsequent crystallization, by the OTR method[18], a secondary goal of this work was to compare the oxygen surface exchange of as-grown amorphous STF films prior to, during, and post crystallization by OTR, ECR, and cross-cell AC-IS for the first time. The electrical/electrochemical methods could provide additional insight into the role of crystallization in oxygen surface exchange. Simultaneous comparison of ECR, cross-cell AC-IS, and OTR on such samples also enables determination of the utility and accuracy of these techniques for amorphous and/or poorly conducting samples, whereas previous comparisons had been limited to oriented, highly crystalline films. Therefore, we performed the comparisons on films grown at different temperatures, with different crystalline quality, in order to cover a range of k values in our comparison. The results show that there is excellent agreement between the k_{chem}

values extracted from the simultaneous OTR and ECR measurements, with evidence pointing to the greater utility of OTR when analyzing surface exchange kinetics for highly resistive and/or amorphous samples. Conversely, we observed considerably less agreement between simultaneous cross-cell AC-IS and OTR measurements of surface exchange coefficients. All the techniques were sensitive to the property changes brought about by *in situ* crystallization, and ECR and OTR detected similar crystallization temperatures.

2. Experimental Methods

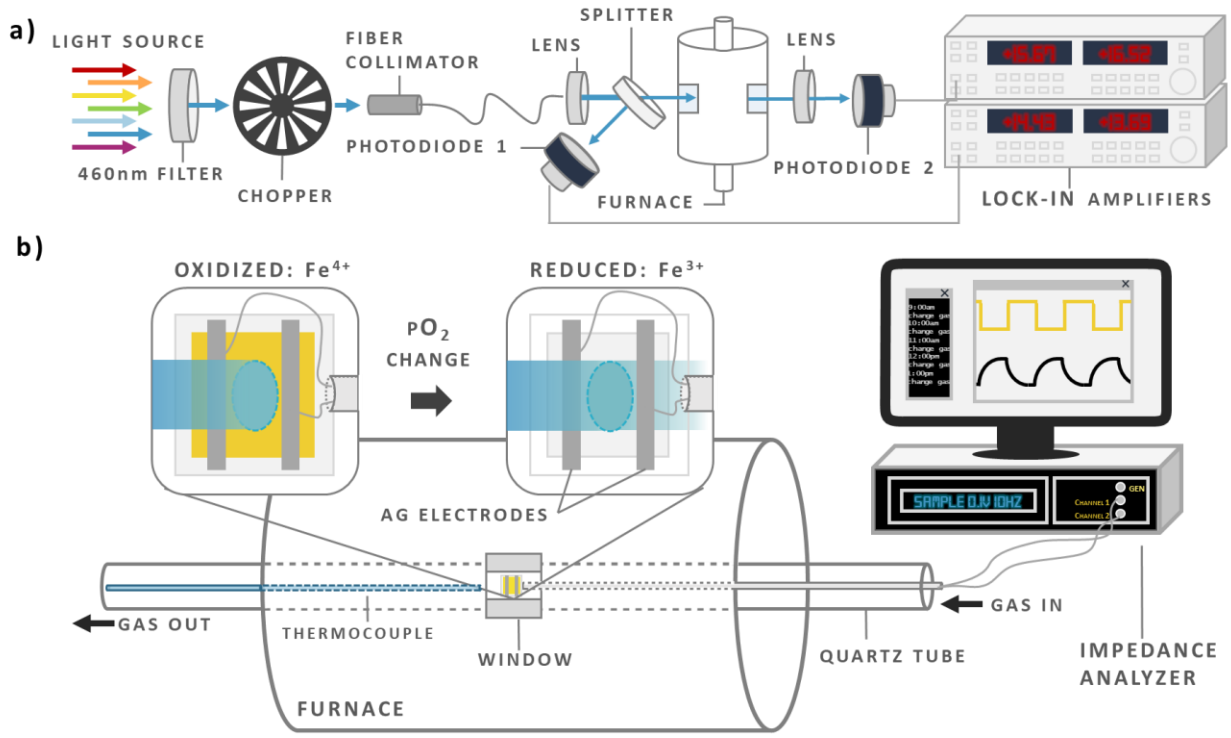

Figure 1. *Simultaneous OTR and ECR setup. a) Light is monochromated, chopped and split before entering the tube furnace. Photodiodes monitor changes in the incident and transmitted light intensity and sync them using a lock-in amplifier. b) As the film is oxidized following rapid step wise changes in the surrounding gas pO_2, the absorbance of the monochromated light increases according to the Beer-Lambert law. Likewise, as the film is reduced, the absorbance decreases.*

2.1 ECR Technique

ECR experiments measure the change in electrical conductivity as a function of time due to oxygen exchange between the mixed conducting STF sample and the ambient gas atmosphere, upon an instantaneous change in oxygen partial pressure (pO2). Under the relatively oxidizing conditions of this work, the electrical conductivity of this p-type mixed conductor is dominated by the electronic contribution.[50] Conductivity changes as a result of pO_2 fluctuations correspond to changes in the hole concentration, caused by oxygen surface exchange and ambipolar diffusion resulting from the imposed gradient in chemical potential of oxygen. Assuming that the hole mobility is independent of the ambient pO_2 over the narrow range used in this study, the changes in hole concentration can be linearly related to the oxygen concentration via the simplified electroneutrality condition appropriate for this pO_2 regime of $SrTi_{1-x}Fe_xO_{3-x/2+\delta}$.[51]

$$2\delta = [p^{\cdot}] / [STF] \quad (1)$$

Therefore, from the normalized relaxation curves of the electrical conductivity, it is possible to extract kinetic parameters, such as the bulk chemical diffusion coefficient (D_{chem}) and/or the chemical surface exchange coefficient (k_{chem}) of oxygen (depending on geometry).

2.2 OTR Technique

Optical transmission relaxation (OTR), which measures the change in transmission of light (at a specific wavelength) when it passes through a material as a result of stepwise oxygen partial pressure changes in the surrounding atmosphere, offers an alternative method to measure the chemical oxygen surface exchange coefficient. The OTR technique has recently been applied to measure kinetics and point defect concentrations in films of the fluorite-structured $Ce_{0.9}Pr_{0.1}O_{2-\delta}$, the perovskites $SrTi_{1-x}Fe_xO_{3-x/2+\delta}$ (x=0.05, 0.10, 0.35) and $SrTi_{0.65}Co_{0.35}O_{3-\delta}$, the Ruddlesden-Popper phase $Sr_2Ti_{0.65}Fe_{0.35}O_{4-\delta}$, and artificial superlattices of $Ce_{0.9}Pr_{0.1}O_{2-\delta}$-$SrTiO_3$[18,21,48,49,52]. Here we will present a brief overview of the nature and origins of optical absorption and its

relationship to oxygen non stoichiometry in non-dilute STF; however, for a more detailed treatment see ref. [51] or the review by Buckner et al.[40] Early work focused on a dilute case: the model system $SrTiO_3$ with dilute Fe on Ti sites. Mossbauer spectroscopy measurements suggested that, in that system, under oxidizing conditions, Fe changes valence from Fe^{3+} to Fe^{4+} as oxygen is added.[53] According to previous work by Maier et al. on single crystals of dilute $SrTiO_3$:Fe, the change in optical absorption at 2.8 eV (~443 nm) appears to be directly proportional to the change in oxidized Fe^{4+} concentration in accordance with the Beer-Lambert law, with Fe^{4+} being the main absorber at this wavelength.[54]

In the present work, we focus on a $SrTi_{0.65}Fe_{0.35}O_{2.825+\delta}$ (STF35) composition with non-dilute Fe, which uses oxygen-deficient STF (containing Fe^{3+}) as the reference state. In this case, the oxidation process can be described as:

$$2Fe_{Fe}^{\times} + v_O^{\bullet\bullet} + \frac{1}{2}O_2(g) \leftrightarrow 2Fe_{Fe}^{\bullet} + O_O^{\times} \quad (2)$$

[50,55]. The generation of holes localized in the vicinity of Fe (i.e., the oxidation of Fe to the "4+" state) electronically charge compensates for the filling of the oxygen vacancies; that is, the change in absorption deriving from of the Fe oxidation relates to the change in oxygen concentration. The relationship between optical absorption change and hole concentration change (and therefore oxygen content change) was shown to be linear using both *ex situ* and *in situ* optical measurements on $Ce_{0.9}Pr_{0.1}O_{2-\delta}$ and $SrTi_{1-x}Fe_xO_{3-x/2+\delta}$ [48,51]. Further, optical relaxations of sufficiently thin samples were shown to lie in, or close to, the "linear regime" (where flux is proportional to driving force), for oxygen partial pressure step changes of the magnitude used in the present work: pO_2 steps between 0.04 atm and 0.21 atm.[21] (In other words, for small pO_2 step sizes, the k values were not significantly dependent on step size, within error.) An explanation of the fitting procedure for the optical relaxation data is given later in this paper.

2.3 Fabrication

STF35 thin films were deposited on 10x10x0.5 mm, single crystal, double side polished substrates (Dalian Keri Optoelectronic Technology Corp., China) using pulsed laser deposition by ablating a dense ceramic target with an excimer laser with a wavelength of 248 nm (PLD: Pascal Corp., Japan, and PLD, Laser: COMPex Pro 50F, Coherent). The substrates were c-plane, (0001)-oriented sapphire (Al_2O_3) for OTR/ECR measurements and (100)-oriented, 13 mol% Y_2O_3 – stabilized ZrO_2 (YSZ) for OTR/cross-cell AC-IS measurements. The internal laser energy was set to 100 mJ with a repetition frequency of 5 Hz, and the laser spot area was about 2-3 mm^2. The substrate and target were rotated continuously during deposition, with the substrate-target distance being approximately 5 cm. The films were deposited at 25 ˚C (amorphous) for the simultaneous cross-cell AC-IS and OTR measurements, and at 400 ˚C (amorphous) and 700 ˚C (crystalline) for simultaneous ECR and OTR measurements, in an O_2 pressure of 5 Pa. The ceramic target used was prepared via a modified Pechini method, and details may be found elsewhere.[56] The growth rate was calibrated using X-ray reflectometry (XRR) and scanning electron microscopy (SEM)[18]. This growth rate calibration was used to determine an approximate thickness of 112 nm for the 25 ˚C-grown film and 100-200 nm for the 700 ˚C-grown film. The thickness of the 400 ˚C-grown film was determined by Rutherford Backscattering Spectrometry (RBS), as described further below, to be approximately 90 nm for the 400 ˚C film, assuming a film density of 4.5 g/cm^3. X-ray Fluorescence analysis of the STF35 target was acquired using an EDX-7000 Energy Dispersive X-ray Fluorescence Spectrometer. The crystalline structure was evaluated by X-ray diffraction (XRD). XRD spectra of post annealed, 400 ˚C grown film were acquired using Bruker D8 Advance XRD System, while the pre crystallization scan was made using XRD system by Rigaku Corp., Japan. *In situ* crystallized films develop a random crystallographic orientation following annealing

at high temperatures, while the high-temperature grown film exhibits two out-of-plane orientations when grown on a (0001)-oriented sapphire substrate (Fig. S3).

2.4 Characterization

2.4.1 RBS

Elemental composition and thickness of STF films were characterized by analysis of RBS data. Measurements were performed at room temperature and under a vacuum of 10^{-6} Torr with a 2 MeV He^+ beam (NEC Pelletron accelerator) incident on the sample. The incident angle, or the angle between the beam and the surface normal, was maintained at 22.5˚ while the backscattered beam exited the sample at an angle of 52.5˚ relative to the surface normal, resulting in a scattering angle of 150˚ between the incident and backscattered beam. Resultant spectra of number of backscattered particles vs. energy were analyzed using SIMNRA software to determine the elemental concentration and thickness of the film. To transform the projected atomic density of the active layer (atoms/cm^2) into film thickness, the density of the film must be known. In this work, the density was assumed to be 4.5 g/cm^3, which is consistent with other STF35 samples deposited under similar PLD conditions and thermal history in our work. The thickness was calculated according to the following equation:

$$\delta_m = \frac{(\sum M_i \varepsilon_i)\theta}{N_A \rho_m} \quad (3)$$

where δ_m is the active layer thickness, M_i represents the molar weight of element i, ε_i is the molar fraction of element i per unit cell, θ is the projected atomic density, N_A is Avogadro's number, and ρ_m is the active layer density.

2.4.2 OTR/ECR

For the simultaneous OTR and ECR measurements, each sample was placed in a quartz tube within a tube furnace with quartz windows to allow light transmission through the sample.

Light was monochromated, chopped, collimated, and split prior to entering the furnace to allow monitoring of the incident light intensity fluctuations with a photodetector ((Light Source, SLA-100A, SIGMAKOKI, Co., Ltd.; Collimator, F230SMA-A, Thorlabs; Chopper, MC2000, Thorlabs; Filter, 442 nm FL441.6-10 filter, Thorlabs). The remaining light was passed through the sample and monitored by a second photodetector (Figure 1). The two photodetector signals were synchronized via lock-in amplifiers, with the ratio of transmitted to incident light used in the analysis.

By rapidly switching the oxygen partial pressure (between 0.04 atm O_2/0.96 atm N_2 and 0.21 atm O_2/0.79 atm N_2) using mass flow controllers, high purity gases, and dessicant columns to create two dry mixed gas streams, and a 4-way valve, the optical transmitted intensity as a function of time was measured and analyzed to extract relevant kinetic values. The relationship between attenuation of light intensity and the absorption coefficient (α) at a specific wavelength follows:

$$\frac{I}{I_0} = e^{-\alpha L} \tag{4}$$

where I is the transmitted light intensity, I_0 is the incident light intensity, and L is the film thickness. From this relation and the dependence of absorption at 2.8 eV on the quantity of Fe^{4+} color centers, the change in concentration of oxygen species as a function of time can be extracted. Further details are given in refs.[18,21] and in Section 3.5.

For the 400 ˚C-grown film, silver paste (Dotite d-550) was applied to serve as strip-shaped current collectors for the in-plane electrical conductivity measurements with an approximately 2 mm space between them to allow for the light beam to pass through that region of the sample unimpeded. For the 700 ˚C-grown film, sputtered Pt current collectors were applied with silver paste used on top to attach the Pt wires to the current collector. The space between the current collectors was approximately 2mm. Platinum wires were fed through the alumina sample holder,

connecting the current collectors to the impedance analyzer (Novocontrol Alpha A). For full in-plane impedance spectra measurements used to determine steady-state conductivities, the frequency range used was between 1 MHz and 0.1 Hz with an applied ac voltage amplitude of 0.1 V. For conductivity relaxations, these were performed at a constant frequency of 10 Hz, where the real impedance corresponded to the dc value of the film in-plane resistance. OTR and ECR measurements were made simultaneously in response to the same pO_2 steps (both oxidizing and reducing); they were repeated as a function of temperature (280 ˚C ≤ T ≤ 580 ˚C) at 50 ˚C intervals on a 400 ˚C, as-deposited amorphous film and in the range (275 ˚C ≤ T ≤ 575 ˚C) at 50 ˚C intervals on an 700 ˚C, as-deposited crystalline film, in order to observe and compare the changes in both optical and electrical relaxation profiles during crystallization and confirm orders of magnitude improvements in k_{chem} as a result of *in situ* crystallization compared to high temperature crystalline grown films.

2.4.3 OTR/ Cross-cell AC-IS

For the cross-cell AC-IS and OTR measurements, half of the 25 °C-grown film surface was left uncoated for the optical measurements, while on the second half a porous Au current collector was applied (Tanaka Kikinzoku International KK high purity Au paste) with a corresponding porous Ag paste counter electrode on the opposite side of the substrate. Isothermal optical and impedance data were collected at ~290 °C, 390 °C, 490 °C, 515 °C, 540 °C, 565°C, and 590 °C for the first measurement run. The sample was then held at 590 °C for ~22 hours in order to compare the aging behavior of the film via OTR and cross-cell AC-IS. A second measurement run was subsequently carried out with isothermal holds at the following temperatures: ~290 °C, 340 °C, 390 °C, 440 °C, 490 °C, 515 °C, and 540 °C. Platinum wires were used to connect the Au current collector and Ag counter-electrode on the electrode half of the film

to the impedance analyzer (see TOC Figure for schematic). For full impedance spectra measurements, the frequency range used was between 10 MHz and 0.01 Hz with an applied ac voltage amplitude of 0.02 V.

3. Results

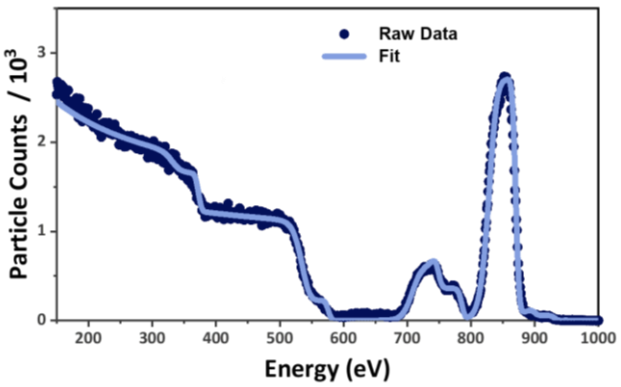

Figure 2. *RBS raw spectra (black dots) and composition and thickness fitting (blue line) of 400 °C-grown film following OTR/ECR measurement.*

3.1 RBS Data

RBS is a powerful tool for analyzing not only thin film thickness and density, but also film and substrate chemical composition. The raw spectra and corresponding fit using SIMNRA software are shown in Figure 2. Large amounts of secondary scattering result in non-zero particle counts between the film and substrate peaks. Peak decay represents surface roughness and porosity within the film, which causes the peaks to be smeared, resulting in the appearance of a shoulder at the lower energy side of the film peaks. Compositional analysis of the 400 ˚C-grown film from the SIMNRA fit is summarized in Table 2 and compared to XRF analysis of the bulk STF35 target. RBS data reveal that there is a slight difference in stoichiometry between the STF thin film and target as well as the presence of trace amounts of contamination, most likely introduced during the

PLD growth process. Although it cannot be definitely concluded from the RBS data, the most likely candidates for contaminants are Ce, Pr, or La, elements found in other targets deposited in the same PLD chamber. A small contribution from residual Ag current collector is also present. Data show there is a slight Sr excess in the film in tandem with a decrease in the Fe/(Fe+Ti) stoichiometric ratio. Precise determination of the oxygen content of the film was unreliable and is therefore not reported here; however, it is clear from analysis of the optical and electrical data that the film exhibits variable oxygen non-stoichiometry depending on temperature and oxygen partial pressure. In order to determine the thickness according to equation (3), a density must be known. The density was assumed to be ~4.4-4.5 g/cm^3 in accordance with XRR data collected on similar samples with the same composition and thermal history. The thickness was subsequently calculated to be about ~90-95 nm.

Table 2. *Calculated film and target stoichiometry using RBS and XRF with stoichiometries normalized to the B-site perovskite concentration (Fe + Ti = 1).*

Element	**Sr**	**Fe**	**Ti**	**Ce/La/Pr**
XRF Target Atomic %	50.1	18.6	31.3	-
XRF Stoichiometry	1	0.36	0.64	-
RBS Film Atomic %	52.1	15.4	32.1	0.4
RBS Stoichiometry	1.09	0.33	0.67	-

3.2 In-plane Impedance and Film Conductivity

Next, we will provide details of the impedance spectra for the in-plane measurements and determination of the in-plane conductivities. The steady state in-plane conductivity was measured as a function of temperature and oxygen pressure for the 400 ˚C-grown, *in situ*-crystallized film on Al_2O_3. Fig. 3a) shows the Nyquist plots of the measured in-plane complex impedance spectra

as a function of temperature for both first and second heating cycles in a pO_2 atmosphere of 0.21 atm. Spectra consisted of a single arc, as expected for in-plane conductivity measurements and seen previously [22].

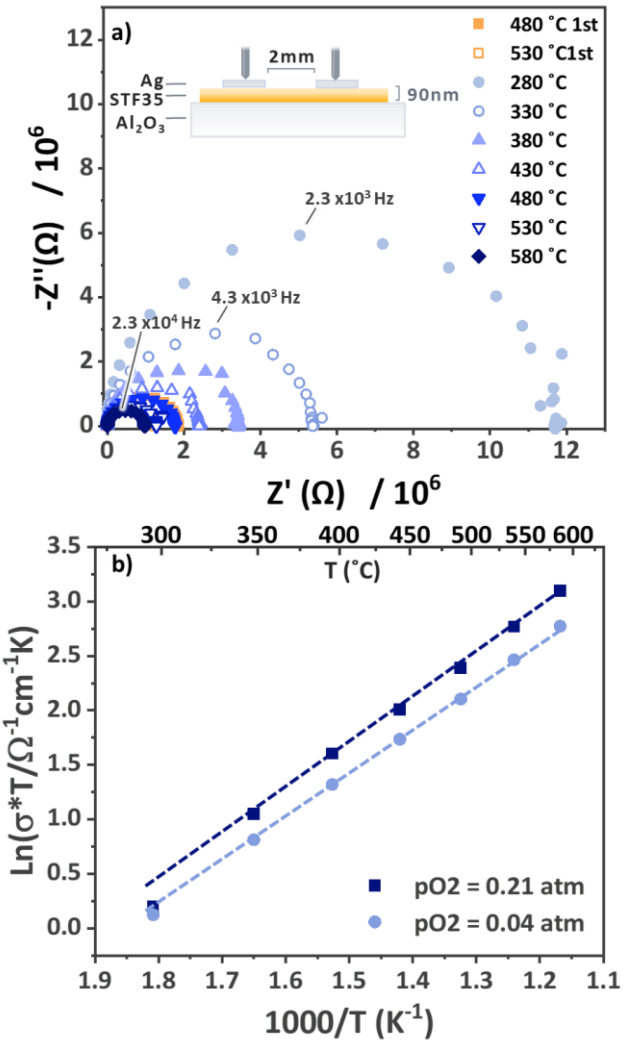

Figure 3: *a) Nyquist plot for the measured in-plane impedance as a function of temperature for the 400 °C grown film on Al_2O_3. Inset schematic of cell configuration. The first two temperature points (480 and 530 °C in orange) refer to measurements taken during the first heating cycle of the amorphous film; no values were obtained at lower temperatures. The rest refer to the measurements taken during the second heating cycle once the film had crystallized, consequently exhibiting measurable impedance at lower temperatures. Select maximum frequency values are labelled. b) Arrhenius plot of in-plane conductivities.*

For the in-plane measurements used in ECR vs. OTR, no impedance was measurable prior to crystallization of the highly resistive 400 ˚C-grown amorphous film at ~470 ˚C; therefore, the measurements for the first cycle include only the 480 ˚C and 530 ˚C temperature points. Once crystallized, the film exhibited measurable resistance values at all temperatures between 280 ˚C and 580 ˚C during the second heating cycle. Measured film thickness and inter-electrode spacing are shown in and Figure 3a) while conductivities determined from the resistances (diameter of the impedance arcs) are shown in Figure 3b); conductivity is higher at the higher pO_2 value due to its predominantly p-type nature. From the steady state conductivity data, the thermal activation energy was determined to be 0.38 ± 0.02 eV and 0.36 ± 0.01 eV for a pO_2 of 0.21 atm and 0.04 atm, respectively. These values are in good agreement with our previously reported value of 0.42 eV in the low temperature (25-500 ˚C) range at 0.21 atm O_2.[22]

3.3 Cross-cell Impedance

Cross-cell complex impedance spectra for the 25 ˚C-grown, *in situ*-crystallized film on YSZ are shown in Supporting Information Figure S1 for the first and second time measurements. We have previously shown that, for this cell geometry and materials set, the low frequency arc corresponds to the STF film/current collector response (surface exchange resistance in parallel with a chemical capacitance and possible interfacial capacitance), while the intermediate and high frequency responses arise from the counter electrode and electrolyte substrate, respectively.[24,57] In the spectra, we can observe the typical shifting of impedance features to higher frequencies with increasing temperature, due to their thermally activated origins. Additionally, here, we observe some irreversible changes and attribute those to the film crystallization and film/current collector aging processes vs. temperature and time, which are superimposed on this thermally activated behavior. When a sufficient portion of the low frequency arc was present to enable equivalent

circuit fitting, we obtained resistance, constant phase element, and corresponding capacitance values for the STF/Au; these raw values are listed in Tables 3-5. Note that the R/k_{chem} values do not decrease/increase exponentially with temperature during the first heating cycle (Table 3), as would be seen for typical thermally activated behavior; the deviation may be related to the crystallization process and possible onset of "aging" at the high temperature point.[18,24] Similarly, the increase in R with time during the subsequent high temperature annealing (Table 4) is attributed to this aging process; corresponding impedance spectra are shown in Supporting Information Figure S2, where the low frequency arc grows over time. Unlike ECR, the cross-cell AC-IS measurements in this frequency range do not allow for determination of R and k_{chem} below 490 ˚C during the second heating cycle (Table 5), due to the high resistance for oxygen surface exchange and incomplete low frequency arcs that preclude precise fitting at lower temperatures. As shown in the tables, the fitted low frequency arc capacitance increases between the first and second heating runs, suggesting a change in the STF film defect and/or interfacial chemistry related to crystallization and/or aging. The constant phase element exponent also increases between the first and second heating runs, indicating more depressed arcs in the first run, which could be related to a broader distribution of time constants and inhomogeneity during the crystallization process. Nonetheless, from these fitted parameters, there is no precise indication of when crystallization occurred

Table 3. *First-time heating fitting parameters (resistance R_p and constant phase element Q & n) and calculated capacitance (C), relaxation time constant (τ), and k_{chem} for the low frequency arc.*

Temp (˚C)	**R_p (Ω)**	**Q**	**n**	**C (F)**	**τ (s)**	**k_{chem} (cm/s)**
488	3.73×10^{4}	1.14×10^{-5}	0.463	4.22×10^{-6}	0.42	2.64×10^{-5}

513	1.61×10^{4}	2.10×10^{-5}	0.504	7.23×10^{-6}	0.34	3.31×10^{-5}
540	5.26×10^{3}	5.29×10^{-5}	0.539	1.77×10^{-5}	0.28	4.03×10^{-5}
565	1.62×10^{3}	1.74×10^{-4}	0.713	1.05×10^{-4}	0.28	3.97×10^{-5}
590	7.61×10^{2}	8.11×10^{-4}	0.706	6.63×10^{-4}	0.62	1.82×10^{-5}

Table 4. *Intermediate anneal fitting parameters (resistance R_p and constant phase element Q & n) and calculated capacitance (C), relaxation time constant (τ), and k_{chem} for the low frequency arc.*

Time (h)	R_p (Ω)	Q	n	C (F)	τ (s)	k_{chem} (cm/s)
0	7.61×10^{2}	8.11×10^{-4}	0.706	6.63×10^{-4}	0.62	1.82×10^{-5}
2	9.02×10^{2}	9.12×10^{-4}	0.696	8.37×10^{-4}	0.82	1.36×10^{-5}
5	1.12×10^{3}	9.95×10^{-4}	0.681	1.05×10^{-3}	1.11	1.01×10^{-5}
10	1.31×10^{3}	1.02×10^{-3}	0.684	1.17×10^{-3}	1.34	8.37×10^{-6}
15	1.48×10^{3}	1.03×10^{-3}	0.688	1.26×10^{-3}	1.53	7.31×10^{-6}
20	1.57×10^{3}	1.04×10^{-3}	0.690	1.30×10^{-3}	1.64	6.82×10^{-6}
22	1.64×10^{3}	1.06×10^{-3}	0.681	1.38×10^{-3}	1.74	6.44×10^{-6}

Table 5. *Second-time heating fitting parameters (resistance R_p and constant phase element Q & n) and calculated capacitance (C), relaxation time constant (τ), and k_{chem} for the low frequency arc.*

Temp (˚C)	R_p (Ω)	Q	n	C (F)	τ (s)	k_{chem} (cm/s)
490	5.04×10^{4}	1.45×10^{-4}	0.784	2.51×10^{-4}	12.67	8.84×10^{-7}
515	1.69×10^{4}	2.06×10^{-4}	0.764	3.03×10^{-4}	5.13	2.18×10^{-6}
540	6.79×10^{3}	3.37×10^{-4}	0.764	4.35×10^{-4}	2.95	3.80×10^{-6}

3.4 Crystallization

The raw data from the simultaneous measurements of optical transmission relaxation and electrical conductivity relaxation on the 400 ˚C-grown film are presented in Figure 4, for first time measurements (4a: ECR, 4c: OTR) and second time measurements (4b: ECR, 4d: OTR). Measurements were made isothermally in the range 280 ˚C ≤ T ≤ 530 ˚C at 50 ˚C intervals, and then repeated once over the temperature range, 280 ˚C ≤ T ≤ 580 ˚C, with light intensity/ conductivity, temperature, and oxygen partial pressure recorded as a function of time. The sample measured was the 400 °C-grown as-deposited amorphous film, to i) confirm whether the two techniques agreed as to the crystallization temperature and ii) compare measurements of k_{chem} over a wide range by both techniques during crystallization. In previous work [18,21], it was observed that a sharp increase in the optical absorption during heating was indicative of crystallization in the films, confirmed by *ex situ* X-ray diffraction, electron microscopy, and electron diffraction. Crystallization of the 400 °C-grown as-deposited film used in this work was confirmed using X-ray diffraction and can be seen in Supporting Information Figure S3.

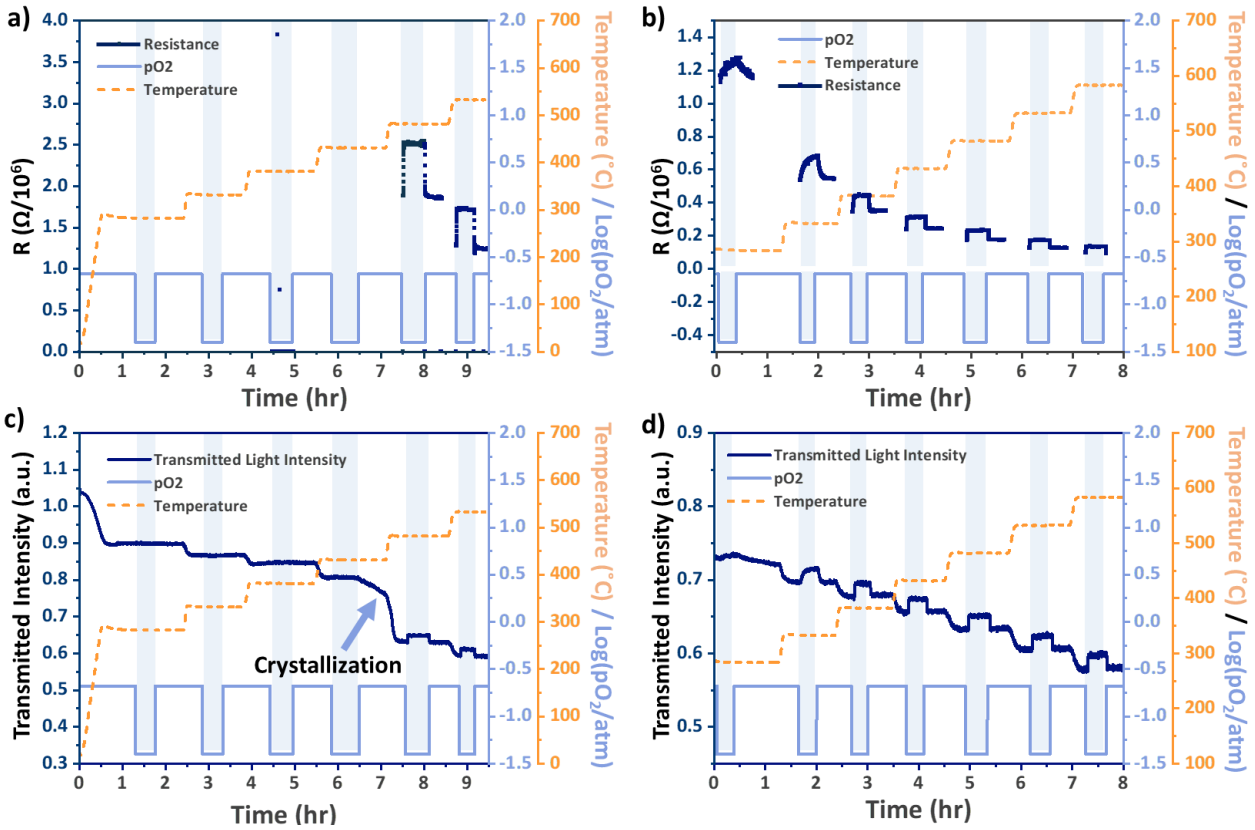

Figure 4. *a), c) Transmitted light intensity, pO_2, and temperature as a function of time for 1st measurement of oxygen reduction/oxidation relaxation of amorphous as-deposited, 400 ˚C-grown film. The arrow indicates the onset of crystallization at ~470 ˚C. b) and d) show the second cycle of measurements of the crystallized film, which exhibited oxygen exchange at 280 ˚C. Shaded regions correspond to a pO_2 of 0.04 atm and white regions to a pO_2 of 0.21 atm.*

In Figure 4, the film is seen to exhibit a rapid decrease in the light transmission at ~450-470 ˚C, corresponding to the crystallization process. The electrical measurements are consistent with this optical behavior, although they provide less information during crystallization. Fig. 4a) shows, by the absence of data, that the amorphous film exhibited resistances that were too high to measure at low temperatures (attributed to a high resistivity combined with a relatively large 2 mm spacing between the electrodes). Once the film reached 470 ˚C, the film resistances were low enough to be measurable. These results suggest that, analogous to the OTR measurements, there was a sharp increase in conductivity, evidenced by a sharp drop in the measured impedance, for

the film as it crystallized. We note that the drop in resistance is not due to simple thermal activation of transport; after crystallization and during the second measurement, the resistance was measurable across the entire temperature range.

Although the exact crystallization point is unclear from the ECR measurements, it appears to occur close to 470 ˚C, based on the appearance of measurable resistance at that point, in excellent agreement with the optical result. The crystallization temperature of this particular film is lower than those of our previously measured films of this composition of ~540-580 ˚C, which may be related to the presence of the current collectors on the surface in the present study or the higher growth temperature (400 ˚C vs. 25 ˚C). A previously grown amorphous film at 400 ˚C, as in this work, exhibited a crystallization temperature of ~500-510 ˚C without current collectors being present, suggesting that increased growth temperatures may lower the eventual crystallization temperature during post-annealing.

The raw optical data from the simultaneous measurements of OTR and cross-cell AC-IS on the 25 ˚C-grown film are presented in Supporting Information Figure S4, for first time measurements and second time measurements. OTR/cross-cell AC-IS measurements were made isothermally at several temperatures in the range 290 ˚C ≤ T ≤ 590 ˚C and then repeated once over the range 290 ˚C ≤ T ≤ 540 ˚C, with light intensity, temperature, and oxygen partial pressure recorded as a function of time. In Figure S4, it is evident that the 25 ˚C-grown sample exhibits a rapid decrease in the transmitted light intensity at ~500-515 ˚C. Therefore, the first measurable optical relaxation occurs at 515 ˚C. In this case, the lower crystallization temperature compared to our previous measurements on 25 ˚C-grown samples might be related to the presence of the Au. A determination of crystallization temperature cannot easily be made from the cross-cell AC-IS data because of the non-continuous nature of the technique, the limited range of k_{chem} values

accessible in the measured frequency range, and the possible contribution of the Au current collector.

3.5 Oxygen Exchange Kinetics

We now turn to comparing the optical and electrical relaxation data, shown in Figure 4. From 280 ˚C ≤ T ≤ 480 ˚C, the 400 ˚C-grown amorphous film exhibited no measurable oxygen exchange in response to steps in pO_2, demonstrated by the constant optical response at each isotherm, even though the data show increases in optical absorption upon increases in temperature. Following crystallization, the film displays rapid optical absorption changes in response to changes in pO_2 at ~480 ˚C and ~530 ˚C. Measurements of oxygen exchange were repeated from 280 ˚C ≤ T ≤ 580 ˚C at 50 ˚C intervals, following cooling of the film to room temperature, to confirm that the film had in fact undergone irreversible changes related to crystallization of the as-grown amorphous film. During this second measurement, the film demonstrated rapid surface exchange in response to the pO_2 steps across the full temperature range. These results are consistent with what we have reported for various *in situ*-crystallized compositions in previous work [18]. The electrical relaxation data are in excellent agreement to these optical relaxation results: once the film crystallized, the sample exhibited rapid resistance changes in response to the pO_2 steps that correspond very well to the optical transmission changes (Fig. 4c)-d) vs. Fig. 4a)-b)). The signal-to-noise ratio is higher in the electrical measurements, but the electrical and optical relaxations take place with similar time constants; the exact fitting will be described further below.

From 290 ˚C ≤ T ≤ 490 ˚C, the 25 ˚C-grown amorphous film also exhibited no measurable oxygen exchange optically in response to steps in pO_2 (fig. S4). Upon crystallization at ~500-515 ˚C, the optical transmission data indicates rapid surface exchange kinetics at ~515 ˚C, ~540 ˚C, ~565 ˚C, and ~590 ˚C. During the second measurement cycle, the film demonstrated an optical

response to changes in pO_2 beginning at 390 ˚C. In contrast, the cross-cell AC-IS data did not exhibit a complete low frequency arc (in the measured frequency range) that would allow for precise k_{chem} fitting until 490 ˚C (fig. S1).

3.6 OTR/ECR/Cross-cell AC-IS Fitting

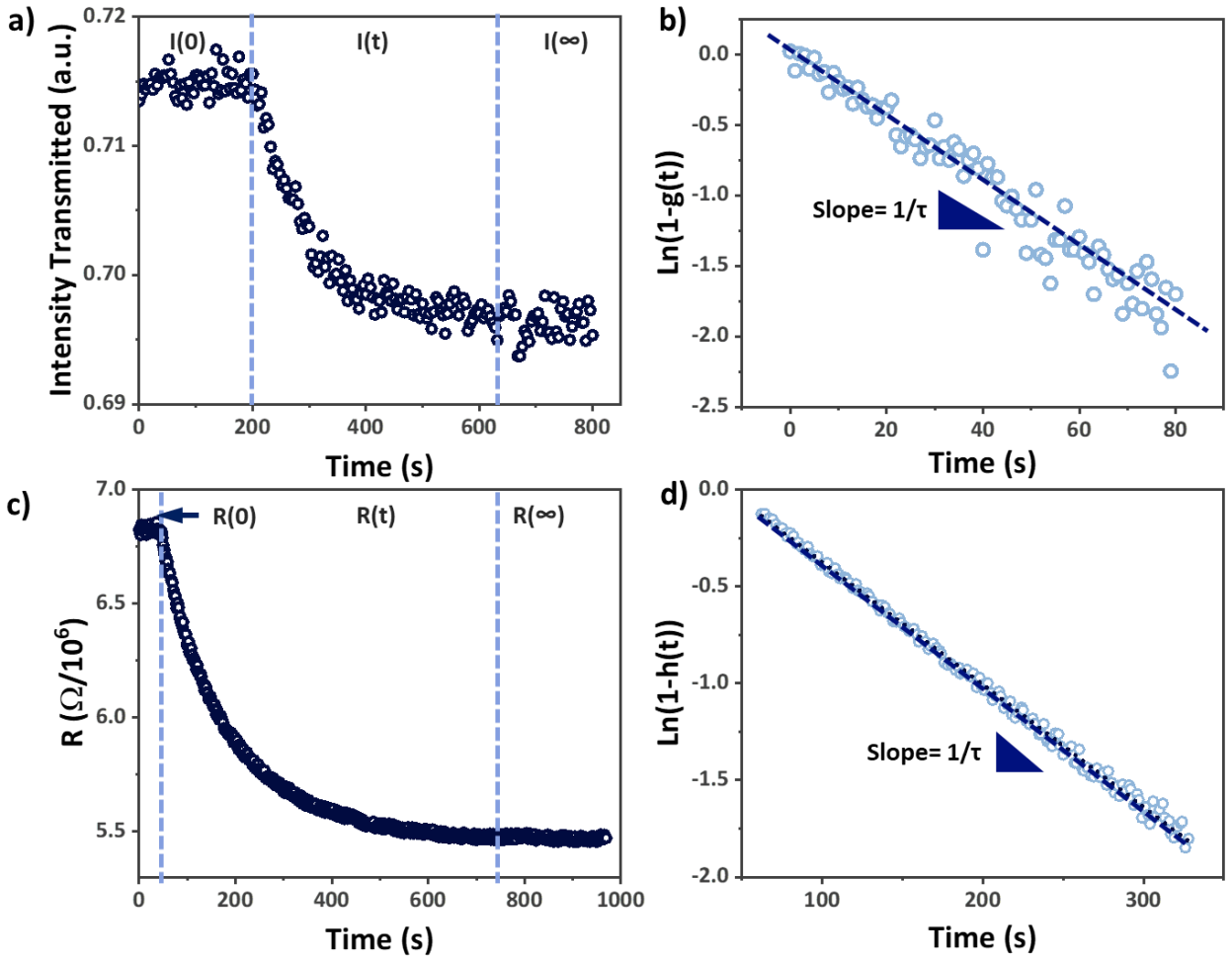

Figure 5: *a) and c) show raw relaxation data for the 400 ˚C-grown film as a function of time for OTR and ECR measurements; b) and d) show corresponding fits of equation (7) to equations (6) and (10) for each technique. The regions between dashed lines in the raw data correspond to values used in solving equations (5) and (9), where I(0) and R(0) indicate the initial values prior to a relaxation event, I(t) and R(t) indicate the value being measured during the relaxation and I(∞) and R(∞) indicate the final value upon equilibration.*

Examples of raw relaxation data of the ratio of transmitted to incident intensity as a function of time and corresponding fits are presented in Figure 5. Surface oxygen exchange coefficients (k_{chem}) were determined from the optical absorption responses upon rapid pO_2 changes from either 0.21 to 0.04 atm O_2 or 0.04 to 0.21 atm O_2. In particular, for a sample of thickness significantly less than the "critical length", $L_c = D/k$, the kinetics are surface exchange-limited, and the relaxation profile can be described by the following analytical solution to Fick's second law (for integrated concentration profiles), allowing determination of k directly:

$$g(t) \equiv \frac{lnI(t)-lnI(0)}{lnI(\infty)-lnI(0)} = 1 - e^{-t/\tau} \tag{5}$$

$$-\frac{t}{\tau} = \ln(1 - g(t)) \tag{6}$$

$$k_{chem} = \frac{L}{\tau} \tag{7}$$

where I_0 is the initial light intensity prior to pO_2 step change, I_f is the final light intensity following the relaxation, I_t is the transmitted light intensity as a function of time, τ is the time constant and L is the thickness of the film. K_{chem} is calculated from fitting the above equation for each oxidation/reduction relaxation.

For the ECR data, a similar fitting procedure was conducted using the following relationship

$$\frac{\sigma(t)-\sigma(0)}{\sigma(\infty)-\sigma(0)} = 1 - e^{-\frac{t}{\tau}} \tag{8}$$

where $\sigma(0)$, $\sigma(t)$, and $\sigma(\infty)$ are the initial, instantaneous and pO_2 equilibrated conductivity, respectively. Equivalently, in terms of the measured low frequency impedance intercept on the real axis, equivalent to the film's dc resistance, R, we can write:

$$h(t) \equiv \frac{1/R(t)-1/R(0)}{1/R(\infty)-1/R(0)} = 1 - e^{-\frac{t}{\tau}} \tag{9}$$

Rearranging, we have

$$-\frac{t}{\tau} = \ln(1 - h(t)) \quad (10)$$

where k_{chem} is equal to the thickness L of the film divided by the slope of the line, τ, as for the optical case above.

For films with surface-exchange limited kinetics, the low frequency (RC) circuit impedance arc in the cross-cell impedance spectrum corresponds to the film (+Au) response. The surface exchange resistance (R) and capacitance (C) (with possible contributions from chemical and interfacial capacitance) were determined by fitting the low frequency impedance arc to an equivalent circuit of a resistor in parallel with a constant phase element (leaky capacitor) using ZView software (Scribner Associates Inc.). The fitted circuit parameters of the (RQ) circuit, shown in Tables 2-4, were used to calculate the true capacitance of the arc according to [58]

$$C = \left(R_p^{1-n} \cdot Q\right)^{1/n} \quad (11)$$

where R_p is the parallel resistance of the low frequency arc, and Q and n are the constant phase element fit parameters. A chemical surface exchange coefficient can be estimated from the time constant ($\tau = R*C$) of the low frequency arc by fitting to equation (7).

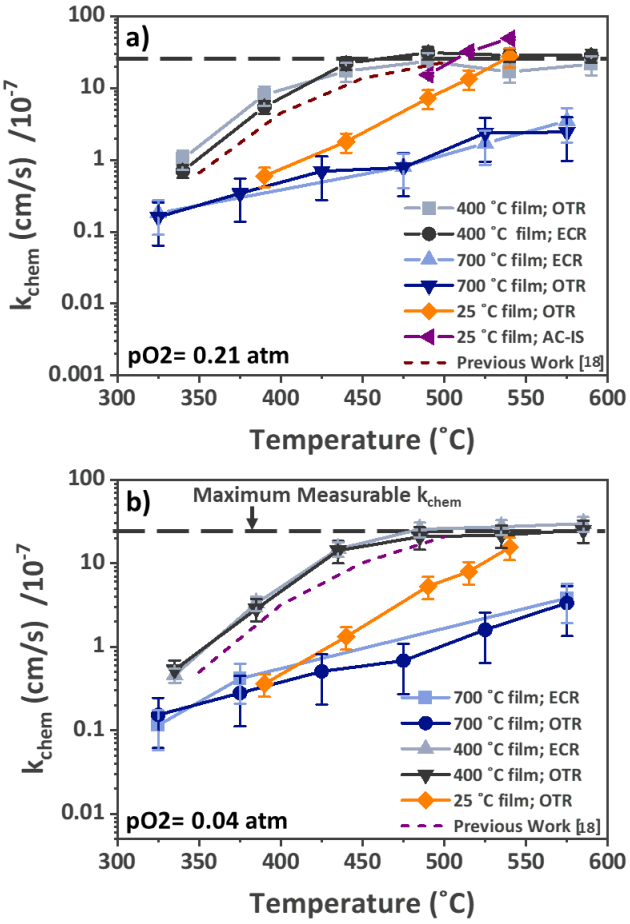

Figure 6. *Fitted k_{chem} from a) oxidation (final pO_2 = 0.21 atm) and b) reduction relaxations (final pO_2 = 0.04 atm) for OTR/ECR/cross-cell AC-IS techniques as a function of measurement temperature. The k_{chem} data shown for the 400 ˚C and 25 ˚C films are taken for the second measurement cycle, while the 700 ˚C film data are taken from the first time measurement. Therefore, all the samples have a slightly different thermal history, with the 25 ˚C being the most post-annealed and the 700 ˚C sample being the least post-annealed. The dashed black lines indicate the maximum measurable k_{chem} for relaxation measurements (OTR & ECR) given a 4s gas flush time for the furnace setup and film thickness according to $k_{chem}=L/t_{flush}$. Short dashed lines indicate relaxations from previous OTR measurements of 400 ˚C grown film.* [18]

Figure 6 shows the oxygen exchange coefficients of the 25 ˚C-grown (second time measurement), 400 ˚C-grown (second time measurement), and 700 ˚C-grown (first time measurement) films. The data directly compare simultaneous OTR vs. ECR k values and near-simultaneous OTR vs. cross-cell AC-IS k values for films with different thermal histories. In

Figure 6a), OTR and ECR k values were determined from fitting the relaxation according to the previous section for pO_2 step changes from 0.04 to 0.21 atm O_2 when the films oxidized. Figure 6b) shows the k_{chem} values extracted for changes in pO_2 from 0.21 to 0.04 atm O_2 when the films reduced. In other words, the pO_2 label indicates the final pO_2 of the relaxation. For cross-cell AC-IS measurements, the pO_2 label indicates the atmosphere during the measurement. From both plots, we can see excellent agreement between the OTR and ECR k_{chem} values as a function of measurement temperature during the 2nd measurement cycle for the 400 ˚C-grown film. Although there are fewer data points for the ECR data measured on the 700 ˚C-grown film, the existing values show equally excellent agreement with those from the OTR data. By contrast, it is unambiguous that the agreement between the cross-cell AC-IS and OTR k_{chem} values is significantly poorer than that of the ECR and OTR measurements of both the 700 ˚C-grown crystalline and 400 ˚C-grown in situ crystallized films. Nonetheless, the cross-cell AC-IS vs. OTR agreement is better than earlier studies on aged, high temperature grown STF35 films, which showed orders of magnitude larger k_{chem} fitted from cross-cell AC-IS measurements.[24]

In line with previous work[18,21], the in situ crystallized films exhibited improved oxygen exchange kinetics when compared to the high temperature crystalline-grown film. It is important to note that the 25 ˚C-grown film had a different thermal history than both the 400 ˚C- and 700 ˚C-grown films (anneal prior to the second measurement), which complicates the direct comparison of the 25 ˚C-grown film k_{chem} values from this cycle to those of the other two films. Therefore, the k_{chem} values extracted from the second measurement cycle of the 25 ˚C-grown film appear artificially lower than they would be given the same thermal history as the other two films.

The horizontal dashed lines in Figure 6a) & b) indicate the upper limit of measurable surface exchange coefficient for relaxation measurements in the experimental setup; it is limited

by the gas flush time (~4 s) [18] and also determined by the thickness of the sample. The high temperature plateau of k_{chem} values seen by OTR and ECR is therefore attributed to the limitations of the experimental design (gas flow rate) and not related to the properties of the material; actual k_{chem} values for those higher temperatures where data fall on the horizontal line are higher than what is plotted. Prior to the samples reaching that limit, i.e., for low temperature measurements, surface exchange activation energies for a pO_2 of 0.21 atm and 0.04 atm were calculated for both ECR and OTR techniques and show good agreement.

Table 6. *Calculated oxygen surface exchange activation energies at a final pO_2 of 0.04 atm and 0.21 atm for the 25 ˚C-, 400 ˚C- and 700 ˚C-grown films.*

Sample	ECR 0.04 atm (eV)	OTR 0.04 atm (eV)	ECR 0.21 atm (eV)	OTR 0.21 atm (eV)	AC-IS 0.21 atm (eV)
25 ˚C-grown	--	1.16 ± 0.03	--	1.18 ± 0.07	1.56 ± 0.18
400 ˚C-grown	1.30 ± 0.05	1.23 ±0.04	1.30 ± 0.09	1.20 ±0.08	--
700 ˚C-grown	0.59 ± 0.07	0.52 ± 0.05	0.49 ± 0.07	0.60 ± 0.09	--

The activation energies for k_{chem} at a final pO_2 of 0.21 atm and 0.04 atm are summarized in table 6. The results from the second heating cycle ECR and OTR measurements on the 400 ˚C-grown film as well as the OTR measurements on the 25 ˚C-grown film are in good agreement within error, as well as with previous work conducted on highly crystalline films (~1.28 eV). [18] However, this is not the case for the cross-cell AC-IS calculated activation energy (1.56 eV), which is higher than expected. Additionally, the activation energies calculated from the ECR and OTR measurements of the 700 ˚C film (~0.6 eV) are consistent with each other but a factor of two lower than expected. The lower activation energy may be caused by a different surface chemistry, given different thermal history, or by the Pt current collectors on the surface of that particular film; for

the 400 °C-grown film they were Ag. The potential impacts of current collectors are discussed further in the following sections.

4. Discussion

4.1 Excellent Agreement Between OTR and ECR

A primary motivation underlying this work was to evaluate the reliability of thin film OTR measurements of k, given prior demonstrated orders of magnitude disagreement between OTR-derived- and cross-cell AC-IS-derived-k values. The results from this work showed that OTR k values, activation energies, and crystallization temperature all agreed with those determined simultaneously by the established ECR technique. At least 3 reasons contribute to this agreement: 1) Both techniques measure changes in properties (electrical conductivity, optical absorption) that are directly proportional to hole concentrations under these relatively oxidizing conditions.[22,51] 2) Both techniques evaluate the same region of the film, although the OTR area is slightly smaller within the larger ECR area; ECR evaluates a rectangular region between the two strip electrodes, and OTR evaluates a circular region where the light beam passes through, also between the electrodes. 3) Both techniques are performed simultaneously in response to the same oxygen partial pressure steps, resulting in the same thermal history, surface chemistry, and driving force for oxygen exchange (discussed further later). One consequence of the agreement is that it supports our earlier OTR results showing a significant increase in oxygen exchange kinetics upon crystallization of STF films and related MIEC films [18,21]. Further, the OTR and ECR k values in this work for the 400 °C-grown film agree very well with our previously measured k values on a similarly-prepared film (see Fig. 6), using OTR without current collectors.[18]

The direct comparison also revealed some differences in capabilities of OTR vs. ECR: OTR results tended to contain more noise, leading to larger uncertainty in the fitted k values. On the other hand, ECR was not at all possible initially at low temperatures on the amorphous films when the resistance was too large (> ~15 MΩ) for the instrument to measure accurately. OTR did enable observation of oxygen exchange kinetics (or the lack thereof) over the full range of conditions studied, including in the high resistance states. To some extent, limitations in either technique can be overcome: Noise in OTR measurements was partially caused by slight contamination on the surface of the laser line filters, which are sensitive to humidity; it may also be lessened by modifying the light intensity, film thickness, and film composition. Excessive resistance hindering ECR measurements can be lessened by placing current collectors closer together or by using interdigitated electrodes; however, close electrode spacing was intentionally avoided in this work in order to evaluate a region of the film away from current collectors and to enable the full light beam to pass through without impinging on current collector regions. The potential influence of current collectors on k values is discussed further later.

4.2 Disagreement of Cross-cell AC-IS

Previous work comparing oxygen surface exchange kinetics in STF35 using nearly simultaneous cross-cell AC-IS and OTR showed large discrepancies in extracted k_{chem} values.[24] For the cross-cell AC-IS measurements, two types of current collectors were used: reactively sputtered porous Pt and painted microporous Au. Regardless of the metal used, the k values (both k_{chem} and k_q corrected by the thermodynamic factor) obtained by cross-cell impedance analysis were 1–3 orders of magnitude higher than those determined optically on the non-coated surface.[24] Furthermore, the cross-cell AC-IS-derived k values deteriorated much more rapidly than OTR k_{chem} values. Similarly, in work performed by Kim et al. on mixed conducting Pr-doped ceria thin

films, cross-plane impedance derived k_{chem} values were found to be 1-2 orders of magnitude higher than those obtained via OTR.

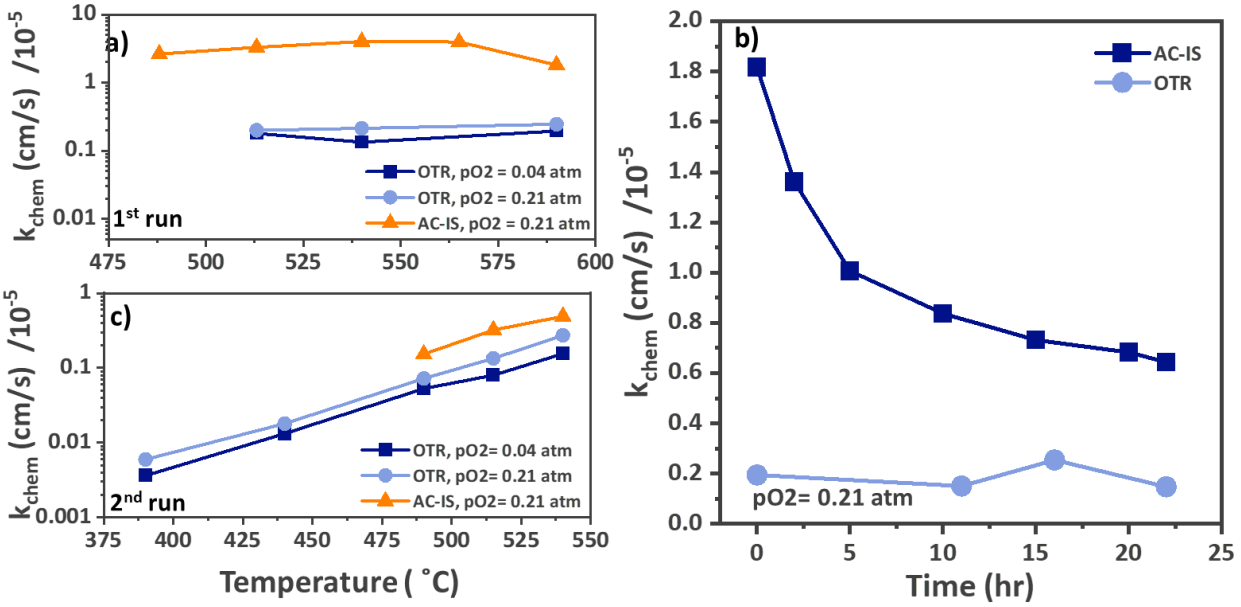

Figure 7. *Fitted k_{chem} for final pO_2 = 0.21 atm and final pO_2 = 0.04 atm for cross-cell AC-IS/OTR techniques a) as a function of measurement temperature for first measurement run, b) as a function of time during intermediate annealing at 590 ˚C, and c) as a function of temperature during second measurement run. Cross-cell AC-IS fitted k_{chem} values are initially an order of magnitude higher than those determined from fitting the OTR data. Cross-cell AC-IS k_{chem} values during annealing reveal a rapid degradation not present in the optical data, which is stable over the entire measurement period of ~22 hours prior to conducting the second measurement cycle. This degradation results in deceptively better agreement during the second measurement run when compared to the first cycle.*

However, in this work, the disagreement between cross-cell AC-IS and OTR k_{chem} values was no more than a factor of 2 during the second measurement cycle. At first glance this appears to reinforce the applicability and accuracy of cross-cell AC-IS, yet the agreement is complicated by the effects of degradation on the apparent cross-cell AC-IS-derived $k_{chem.}$ In figure 7a), comparison of the k_{chem} values from the first measurement cycle, during which the film crystallizes

and subsequently displays measurable surface exchange, show that the cross-cell AC-IS k_{chem} values are an order of magnitude higher than those extracted from the optical data. This difference shrinks during the second measurement cycle to roughly a factor of two, as seen in figure 7 c). Figure 7 b) shows the intermediate isothermal anneal conducted at 590 ˚C for ~22 hours, following the first measurement cycle and prior to the second. It is clear from these data that the cross-cell AC-IS k_{chem} values degrade sharply, whereas the optically derived k_{chem} values show no such comparable decrease. Therefore, the supposed better agreement in the second measurement cycle may in fact be coincidental and due to the degradation rather than representing a true film k_{chem}. It cannot be said with any certainty, then, that the values prior to, or following, the sharp decrease in cross-cell AC-IS k_{chem} during the isothermal hold represent the true material property under study. The origin of the degradation was not determined in this work, but as noted above, similar degradation of cross-cell AC-IS values, not observed optically, has been attributed to the current collectors in our previous work. In the following subsections (4.2.1-4.2.2), we consider some possible reasons for the disagreement of the cross-plane AC-IS results vs. ECR and OTR results on the *in situ* crystallized STF films. Some aspects of these considerations have been raised in our earlier work.[24,40,48]

4.2.1 Driving Forces

The driving forces for oxygen exchange in cross-cell AC-IS and OTR/ECR are fundamentally different. The generalized driving force for transport and reactions involving both ions and electronic species is an electrochemical potential gradient, with contributions possible from an electrical potential gradient and/or a chemical potential gradient. ECR and OTR rely on measurement of the hole concentration change, integrated throughout the volume under testing, in response to an oxygen chemical potential gradient introduced following a stepwise change in the

surrounding atmosphere. In contrast, cross-cell AC-IS relies upon an oscillating electrical potential gradient (AC sinusoidal voltage), perpendicular to the film surface, and introduced between the current collectors, while the surrounding gas atmosphere remains constant. Therefore, it is not the hole concentration change in the time domain in response to the oxygen partial pressure step that is being measured directly via cross-cell AC-IS; rather, it is the complex impedance in the frequency domain through the whole cell. At low enough frequencies, oxygen can exchange across the MIEC surface in response to the applied electrical potential gradient, and the characteristic frequency of the low-frequency impedance feature is directly proportional to k_{chem}. (This frequency is inversely proportional to the time constant ($\omega=1/\tau$), which is the product of the resistance to surface exchange and the chemical capacitance of the MIEC from storing oxygen ($\tau= R \cdot C$)). This fundamental difference in driving force may theoretically contribute to the differing k values obtained from cross-plane AC-IS vs. OTR and ECR, as discussed below.

The difference in driving force (chemical vs. electrical) may contribute to a different atomistic mechanism or rate-limiting step for oxygen exchange. For the perovskite STF, the activation energy for oxygen surface exchange (k_q) as a function of Fe concentration was shown to correlate to the calculated position of the Fermi level relative to the conduction band, suggesting that availability of electrons may be rate limiting in this p-type MIEC.[25,59] In addition, for dilute Fe-substituted $SrTiO_3$, electron transfer to adsorbed oxygen has been suggested as a possible rate-limiting step [12,54,60]. It can be theorized then that the applied electrical driving force may alter the space charge region or the possible Schottky barrier at the current collector-oxide interface (metal-semiconductor interface), with consequences for electron transfer at the interface and changes to the surface defect chemistry.[61,62] Electronic carrier injection from the current collectors may artificially increase the local Fermi level resulting in exaggerated k_{chem} values. Direct transfer of

electrons from current collectors to adsorbed oxygen could also occur. OTR and ECR measurements instead depend on the oxygen chemical potential gradient between the film and the surrounding gas atmosphere to drive the oxygen exchange reaction, Even in the hypothetical absence of current collectors, the cross-plane electric field unique to cross-plane AC-IS measurements and voltage drop across the film-gas surface could modify the mixed conductor's surface chemistry compared to a situation with no applied field in that direction. Therefore, it is likely that the k_{chem} values obtained using OTR and ECR more accurately represent the native oxygen exchange rate of the material under study, and greater caution should be given in the future to applying or interpreting cross plane AC-IS to mixed conductors with limited electronic conductivity. The k_{chem} values obtained in this simultaneous comparison of ECR and OTR on STF35 show excellent agreement, which is not seen when comparing cross-cell impedance based k_{chem} values with any other technique, be it IEDP, ECR or OTR. This result further strengthens the validity and accuracy of OTR as a novel technique for understanding surface oxygen exchange kinetics in optically active materials without the need for current collectors.

4.2.2 Use of Current Collectors

In addition to the differing driving forces that underpin cross-plane AC-IS and ECR/OTR, the presence of current collectors themselves may cause significant alterations to the obtained k_{chem} values. There are several possible mechanisms by which current collectors may affect $k_{chem,}$ which will be discussed in the following text, namely, a) impurity gettering/ impurity donation, b) formation of triple-phase regions, c) catalytic effects, and d) current collector migration/ instability.

a) impurity gettering or impurity source

It is possible that the current collectors could modify impurity adsorption behavior on the film surface through impurity gettering, thus reducing the impurity-driven degradation of the film's surface exchange kinetics. For example, Bishop et al. found considerable concentrations of extrinsic impurities (Si, K, Na, and Ca) deposited on the surface of (Pr,Ce)$O_{2-\delta}$ films following optical absorption measurements at high temperature[35], which the authors hypothesized could be partly responsible for the higher cross-plane AC-IS k_{chem} values when compared to the OTR values.[26] For extrinsic impurities that reach the film surface through the gas phase, it is possible that the electrodes "capture" these impurities, through adsorption or reaction, before they reach the film, thereby protecting the covered film surface. Alternatively, it should be noted that current collectors containing binders or impurities could contribute to the opposite effect of poisoning the surface if those impurities diffuse onto the film of interest.

b) triple-phase sites

The triple-phase boundary (TPB) sites between the film, current collector, and gas phase may have faster oxygen exchange kinetics relative to the native film surface, and therefore the overall k value obtained may be dominated by exchange kinetics at the TPBs and not at the film surface alone. STF, in particular, has a lower electronic conductivity than many mixed conductors, and the presence of highly electronically conducting current collectors may enable more active TPB sites. The benefit to k values may scale with the area of the film surface in close proximity to the metal, and consequently this effect may be responsible for the large differences seen when comparing cross-cell AC-IS and OTR, particularly in previous work, where the full film surface was painted or sputtered for cross-cell AC-IS. In other words, the effect of the metal may extend only a limited distance into the film. In the ECR measurements of the 400 °C-grown film, two strips of widely spaced current collector were present on the film surface, but not in the region

being probed, which lay between the metal strips. In this case, the presence of current collectors does not seem to have had a large effect on the k_{chem} values obtained in this work as evinced by the excellent agreement (shown in Figure 6) with previous OTR measurements on a film grown under the same PLD conditions but with no current collectors. In a study of the TPB between a $La_{0.6}Sr_{0.4}CoO_{3-\delta}$ (LSC) mixed conductor and $Ce_{0.9}Gd_{0.1}O_{1.95}$ (GDC) ionic conductor, Fujimaki et al. showed that the oxygen exchange reaction took place within 60-70 μm of the interface and that the effective reaction area decreased (vs. pure LSC) by the introduction of the TPBs with GDC. [63,64] That work supports the idea that even for a good mixed conductor, TPBs can modify the oxygen exchange kinetics and pathway.

c) catalytic effect

For individual metals, the oxygen exchange kinetics apparently follow the trend: Ag > Au > Pt, with Ag having the lowest activation energy and Pt having a higher activation energy than STF35 for surface exchange (1.67 eV for Pt vs. 1.20-1.30 eV for STF in this work). [65] Nonetheless, the effect of these metals may be different when applied on top of STF35 and could depend on particle size. For example, Leonhardt et al. measured large increases in k_{chem}, measured by optical absorption spectroscopy, upon coating Fe doped single crystals of $SrTiO_3$ with Pt, Ag, and Cr. However, this enhancement in k and corresponding reduction in activation energy was not seen in surface tracer exchange measurements of k*, implying that the metals increase the availability of electrons (and not tracer incorporation) for surface exchange. The metal layer thus merely blocks active sites on the native surface, resulting in a small negative effect on k*.[66] There are several examples in the literature of the benefit of Ag on cathode performance in SOFCs using other MIECs, primarily due to the reduction in the electrode ohmic resistance and enhancement of the catalytic O_2 reduction activity, for example, Ag coatings on $Ba_{0.5}Sr_{0.5}Co_{0.6}Fe_{0.4}O_{3-\delta}$ [67] and Ag

nanoparticles infiltrated into a porous $La_{0.6}Sr_{0.4}Co_xFe_{1-x}O_{3-\delta}$ (x = 0.2)- $Ce_{0.9}Gd0.1O_{1.95}$ cathode. [68] Guo et al. also studied the contribution of Ag and Au current collectors to the performance of a $Ba_{0.5}Sr_{0.5}Co_{0.8}Fe_{0.2}O_{3-\delta}$ (BSCF) electrode on a Sm-doped CeO_2 electrolyte.[69] The use of Ag as the current collector yielded lower area-specific resistance and improved cell performance compared to a cell with a Au current collector, although it is not clear how the presence of Au or Ag compared to a sample with no current collector present. The activation energy for oxygen reduction over the BSCF electrode was reduced by applying the silver current collector, which the authors hypothesized was due to faster oxygen surface diffusion.

d) current collector instability

In our previous work, the metal current collectors for cross-cell AC-IS led to long-term degradation of k_{chem} and k_q over time, a decline not seen to the same extent in the optical measurements.[24] The decrease in k was about 1-2 orders of magnitude and attributed to degradation of the Pt current collectors themselves, since the counter-electrodes, fabricated from the same porous Pt showed the same degradation. Some instability of the current collectors was similarly evinced in the current work. As shown in Fig. 7, cross-cell AC-IS k values rapidly degraded over time during an isothermal anneal, while the OTR k values remained stable. For ECR on the 400 °C-grown film, although Ag paste was applied instead of Au or reactively sputtered Pt (as used for cross-cell AC-IS), the metal current collectors did eventually start to delaminate from the STF35 film, potentially indicating poor surface adhesion and electrical contact after protracted time at high temperatures. Nonetheless, no detrimental effects to the ECR-derived k_{chem} values were observed in the relatively short measurement time in this work. ECR only requires maintaining a consistent area *between* the current collectors (this is the region under test) during a given

relaxation; unlike cross-cell AC-IS, it is not sensitive to the precise contact area between current collectors and film.

4.3 Uncertainty in k_{chem}

Large discrepancies in extracted k_{chem} found in the literature, as outlined in the section 1, may arise from unintentional differences in film surface chemistry and microstructure, film thickness, synthesis route, contamination due to handling and storage, and measurement conditions such as impurity gases, thermal history, electrical history, and dwell time. In the present work, we eliminated those variations through simultaneous measurements; however, there are other sources that contributed to some uncertainty in the extracted k values. There are thickness variations across the film (±5 nm according to RBS measurements in different locations), but we expect that these differences are inconsequential due to the measurements being conducted over essentially the same region of the same film and this variation being small relative to the average film thickness used in the analysis. Therefore, we expect that the majority of the uncertainty is due to the fitting procedure itself, with optical measurements resulting in increased uncertainty due to data points being taken every 4 seconds for each relaxation compared to every 1 second for the conductivity measurements. Similarly, the signal-to-noise ratio for the OTR measured intensity is smaller than that of the ECR measured conductivity. The uncertainties of the k_{chem} values ranged from 20-30% in this work, which is similar to the estimated 20% used in our previous work. These uncertainties were due to the fitting procedure, uncertainty due to noise, as well as thickness variation.

4.4 Maximum Measurable k_{chem} Value

Previously, the gas flush time for our optical transmission relaxation setup was determined to be about 4 seconds.[18] The 4 second gas flush time results in a maximum possible measurable time constant of 4 seconds and consequently a derived k_{chem} of ~2.25×10^{-6} cm/s given a 90 nm

thickness for the 400 °C-grown film in this work ($k_{chem}=L/\tau$). This maximum measured value is represented by a dotted line in Figure 6. It is clear that by 480 ˚C, the maximum measured value is reached, indicating that these k_{chem} values are likely higher than those shown in the plot. However, it remains that the k_{chem} values obtained from both OTR and ECR techniques show excellent agreement below 480 ˚C as well as at temperature points above 480 ˚C, where relaxations become gas flush time-limited. Cross-cell AC-IS is not subject to this limitation.

4.5 Effect of Crystallization

The purpose of this work was not only to reconcile the large discrepancies in k_{chem} found in the literature when comparing the same materials, but also to compare ECR, cross-cell AC-IS and OTR over a wide range of k values during the dynamic restructuring of STF35 as it undergoes thermally activated crystallization. When heated to above ~500 °C, the STF35 as-grown amorphous films in the present study suddenly and irreversibly exhibited rapid oxygen surface exchange ability, as seen in the relaxation profiles upon changing oxygen partial pressure. This sudden onset of oxygen exchange followed by continuing exchange during subsequent heating cycles even at low temperatures (280 ˚C), suggests irreversible structural and defect chemistry changes in the STF film. These changes were observed optically, electrically, and electrochemically, and the OTR and ECR results were in excellent agreement. Further, the cross-cell AC-IS results also showed significant changes in the impedance spectra as a result of crystallization, such as higher capacitance and less arc depression. We emphasize that, to our knowledge, this work is the first time that the effect of crystallization on k_{chem} values has been observed *in situ* electrically and electrochemically. In previous work, we demonstrated by *in situ* OTR that an increase in k values occurs due to crystallization.[18,21] In the present work, ECR and OTR methods also agreed as to the apparent crystallization temperature, signaled by a significant

increase in both optical absorption and electrical conductivity. Thus, the new ECR results confirm the OTR results in the present study and also those that we had previously measured. When comparing the results obtained in this study with our previous work conducted on a similar post-annealed STF35 grown at 400 ˚C, the OTR-derived k_{chem} values show good reproducibility (e.g., previous k_{chem} values were ~$2.5x10^{-7}$ cm/s, ~$9.5x10^{-7}$ cm/s and ~$2.5x10^{-6}$ cm/s vs. $2.9x10^{-7}$ cm/s, ~$1.2x10^{-6}$ cm/s and $2.3x10^{-6}$ cm/s in the current work at 400 ˚C, 450 ˚C and 500 ˚C, respectively).[18] Given that there are possible differences between these two samples in terms of film surface area and porosity (due to the stochastic nature of the apparently homogeneous crystallization process) along with any surface contamination and film stoichiometry differences, which can give rise to large variations in k_{chem} between different films with nominally the same compositions, it is promising that the results here almost exactly agree with previous work. This agreement lends strong support to the accuracy of OTR in determining the true k_{chem} of a native material surface.

Our previous work analyzing the microstructure of *in situ* crystallized films via SEM and TEM indicated the formation of gas channels, as well as the presence of crystalline and porous regions within the bulk of the film.[18] These changes were attributed to a densification and dynamic restructuring of the film concurrent with crystallization, as the larger amorphous network contracted to form a crystalline lattice. Because of the additional surface area present in the *in situ*-crystallized films, it is in principle possible that there could be a disparity between the effective oxygen exchange rate (including morphological factors such as porosity, gas channels, and thickness variations) determined in this work and the true exchange rate of the material. On the other hand, we did adjust k_{chem} in prior work to account for the estimated ~3x increase in surface area and still found that it was strongly enhanced by orders of magnitude around the crystallization point. Therefore, in spite of the increased surface area and the occasional development of triple-

phase boundaries between the gas atmosphere, electrode and electrolyte in some of the crystallized films, we suggest that the oxidation of the film ($Fe^{3+} \rightarrow Fe^{4+}$), which leads to the increase of its optical absorption and electronic conductivity, may be a more significant factor responsible for the appearance of rapid oxygen exchange in STF35 films upon crystallization. Similarly, the emergence of pristine surfaces devoid of deleterious Sr enrichment may result in increased surface activity relative to as-grown crystalline films. Further work is ongoing to investigate the mechanisms.

Previous work showed not only the benefits of *in situ* crystallization for k_{chem} in STF35 but found similar results in the related perovskite $SrTi_{0.65}Co_{0.35}O_{3-x}$, (STC35) and the Ruddlesden-Popper phase $Sr_2Ti_{0.65}Fe_{0.35}O_{4-d}$ (RP-STF35).[18,21] Each of these compositions exhibited at least a 2 orders of magnitude difference in k_{chem} between post-annealed amorphous films and high temperature-grown crystalline films, indicating the benefit of low temperature processing and *in situ* crystallization on oxygen exchange kinetics in STF35, STC35 and RP-STF35.

5. Summary and Conclusions

This work, for the first time, compared the oxygen surface exchange coefficients obtained from simultaneous ECR and OTR measurements on the mixed ionic and electronic conductor STF35 in the temperature range 300-600 ˚C. An as-grown amorphous film (400 ˚C) was crystallized *in situ* in order to better understand the applicability and validity of OTR and ECR techniques in the context of dynamic hierarchical restructuring in MIECs as well as in highly resistive amorphous films; a crystalline 700 ˚C-grown film was also compared to broaden comparisons to a different microstructure and corresponding range of k values. Further, near-simultaneous cross-cell AC-IS and OTR measurements were conducted on as-deposited amorphous film (25 ˚C) before, during, and after crystallization to ascertain whether the

previously-observed orders of magnitude discrepancy in acquired k_{chem} values for these techniques would also be present in STF35 films that did not suffer extensive aging and correspondingly low k values. A secondary goal was for ECR and cross-cell AC-IS to provide further insight into the *in situ* crystallization process.

Results are summarized as follows: 1) The as-grown amorphous STF35 film crystallized at ~470 ˚C (400 ˚C-grown film), which is significantly lower than for the 25 ˚C grown film (~500-515 ˚C), as well as for what is typically seen for this composition when grown at 25 ˚C (~550 °C), indicating the possible role of the relatively high growth temperature in facilitating post-annealing-induced crystallization of the film. 2) Activation energy and k_{chem} values for the 400 ˚C-grown film with widely-spaced current collectors were in excellent agreement with previous work where no current collectors were applied. 3) Activation energy and k_{chem} values obtained by simultaneous ECR and OTR on both 700 ˚C- and 400 ˚C-grown films were the same for both techniques, within error, though OTR values exhibited greater uncertainty due to lower signal-to-noise ratio. 4) OTR enabled determination of k_{chem} in highly resistive, optically active thin films where ECR and cross-cell AC-IS did not. 5) OTR permitted measurement of the native oxide surface behavior without the need for current collectors which, in the context of cross-cell AC-IS measurements, were shown to both increase the apparent k values as well as cause significantly accelerated deterioration of apparent k over time. 6) All methods were sensitive to the crystallization process, with OTR detecting dramatic increases in optical absorption, ECR detecting significant increases in sample electrical conductance, and cross-cell AC-IS detecting increases in capacitance and constant phase element exponent; however, only OTR and ECR displayed the continuous monitoring and precision able to detect the crystallization temperature, with good agreement. 7) Cross-cell AC-IS/OTR k_{chem} values of the 25 ˚C-grown film showed poorer agreement than those of the

ECR/OTR measurements during both first-time (one order of magnitude difference) and second-time measurements (factor of two difference).

This discrepancy from cross-cell AC-IS suggests an important role of the current collector and/or driving force for oxygen surface exchange. For example, the current collector may help to overcome the possible rate-limiting role of electronic charge transfer for oxygen surface exchange in STF. It can be theorized from this study that current collectors may play a more significant role in assisting surface exchange for films with poor surface electronic transfer, e.g., those with a higher degree of Sr segregation, which hinders the charge transfer at the oxide surface (acts as a tunnel barrier and modifies surface electronic structure [15]). This effect may explain the smaller discrepancy observed in cross-cell AC-IS vs. OTR for more pristine films in the present study vs. the highly aged films in our prior study. In a broader sense, the work presented here indicates that caution must be taken in applying cross-cell impedance-based techniques for the determination of oxygen exchange kinetics in MIEC thin films, owing to the presence of current collectors as well as the differing driving forces between techniques that may result in alterations to the rate-limiting step in the oxygen exchange reaction. By contrast, the established ECR method in this work directly validated the results of OTR, clarifying that OTR is an accurate technique for the study of native surface reaction kinetics.

ASSOCIATED CONTENT

Supporting Information.

Cross-cell impedance data of 25 ˚C-grown film; cross-cell impedance data of 25 ˚C-grown film during anneal; measured X-ray diffraction pattern for 400 ˚C-grown film; in situ optical transmitted

light intensity of 25 °C-grown film; in situ optical transmitted light intensity of 700 °C-grown film; Activation energy of 700 ˚C- and 25 ˚C-grown films. (Figures S1−S6)

25 ˚C-grown film fitted k_{chem} values; 700 ˚C-grown film fitted k_{chem} values; 400 ˚C-grown film fitted k_{chem} values. (Tables S1−S3)

The following files are available free of charge.

Supporting Information (PDF)

AUTHOR INFORMATION

Corresponding Author

* Corresponding author email: nhperry@illinois.edu

Present Addresses

† Present affiliation: Toyota Motor Engineering & Manufacturing (China) Co., Ltd, Dongsihuang Road No.55, Changshu, Jiangsu, China

Author Contributions

‡ These authors contributed equally

Funding Sources

U.S. Department of Energy, Basic Energy Sciences (grant # DE-SC0018963). IIE-GIRE Fellowship (supported by NSF, under grant no. 1829436)

ACKNOWLEDGMENT

NHP and EJS gratefully acknowledge financial support from the U.S. Department of Energy, Basic Energy Sciences through a DOE Early Career Award (grant # DE-SC0018963). EJS

acknowledges an IIE-GIRE Fellowship (supported by NSF, under grant no. 1829436) that supported a research exchange visit to Kyushu University to enhance collaboration on this work. Structural and chemical analysis of films was carried out in the Materials Research Laboratory Central Research Facilities, University of Illinois. EJS and TC also acknowledge the International Institute for Carbon-Neutral Energy Research (WPI-I2CNER), supported by MEXT, Japan.

ABBREVIATIONS

OTR, optical transmission relaxation; ECR, electrical conductivity relaxation; AC-IS, ac impedance spectroscopy; MIEC, mixed ionic electronic conductor; STF, $SrTi_{1-x}Fe_xO_{3-x/2+\delta}$;

REFERENCES

[1] Bredesen, R.; Mertins, F.; Norby, T. Measurements of Surface Exchange Kinetics and Chemical Diffusion in Dense Oxygen Selective Membranes. Catal. Today 2000, 56 (1), 315–324.

[2] Liu, Y.; Baumann, S.; Schulze-Küppers, F.; Mueller, D.; Guillon, O. Co and Fe Co-Doping Influence on Functional Properties of SrTiO3 for Use as Oxygen Transport Membranes. J. Eur. Ceram. Soc. 2018, 38, 5058-5066.

[3] Schulze-Küppers, F.; Ten Donkelaar, S. F. P.; Baumann, S.; Prigorodov, P.; Sohn, Y. J.; Bouwmeester, H. J. M.; Meulenberg, W. A.; Guillon, O. Structural and Functional Properties of SrTi1−xFexO3−δ (0⩽x⩽1) for the Use as Oxygen Transport Membrane. Sep. Purif. Technol. 2015, 147, 414–421.

[4] Sunarso, J.; Baumann, S.; Serra, J. M.; Meulenberg, W. A.; Liu, S.; Lin, J.; da Costa, J. C. D. Mixed Ionic-Electronic Conducting (MIEC) Ceramic-Based Membranes for Oxygen Separation. J. Membr. Sci. 2008, 320 (1–2), 13–41.

[5] Menesklou, W.; Schreiner, H.; Härdtl, K. H.; Ivers-Tiffée, E. High Temperature Oxygen Sensors Based on Doped SrTiO3. Sens. Actuators B Chem. 1999, 59 (2), 184–189.

[6] Rothschild, A.; Litzelman, S. J.; Tuller, H. L.; Menesklou, W.; Schneider, T.; Ivers-Tiffée, E. Temperature-Independent Resistive Oxygen Sensors Based on SrTi1−xFexO3−δ Solid Solutions. Sens. Actuators B Chem. 2005, 108 (1), 223–230.

[7] Baumann, F. S.; Fleig, J.; Cristiani, G.; Stuhlhofer, B.; Habermeier, H. U.; Maier, J. Quantitative Comparison of Mixed Conducting SOFC Cathode Materials by Means of Thin Film Model Electrodes. J. Electrochem. Soc. 2007, 154 (9), B931.

[8] Jacobson, A. J. Materials for Solid Oxide Fuel Cells. Chem. Mater. 2010, 22 (3), 660–674.

[9] Adler, S. B. Factors Governing Oxygen Reduction in Solid Oxide Fuel Cell Cathodes. Chem. Rev. 2004, 104 (10), 4791–4844.

[10] Graves, C.; Ebbesen, S. D.; Jensen, S. H.; Simonsen, S. B.; Mogensen, M. B. Eliminating Degradation in Solid Oxide Electrochemical Cells by Reversible Operation. Nat. Mater. 2015, 14 (2), 239–244.

[11] Laguna-Bercero, M. A. Recent Advances in High Temperature Electrolysis Using Solid Oxide Fuel Cells: A Review. J. Power Sources 2012, 203, 4–16.

[12] Maier, J. Physical Chemistry of Ionic Materials: Ions and Electrons in Solids; John Wiley & Sons, 2004.

[13] Tietz, F.; Sebold, D.; Brisse, A.; Schefold, J. Degradation Phenomena in a Solid Oxide Electrolysis Cell after 9000 h of Operation. J. Power Sources 2013, 223, 129–135.

[14] Shao, Z.; Haile, S. M. A High-Performance Cathode for the next Generation of Solid-Oxide Fuel Cells. Nature 2004, 431 (7005), 170–173.

[15] Chen, Y.; Jung, W.; Cai, Z.; Kim, J. J.; Tuller, H. L.; Yildiz, B. Impact of Sr Segregation on the Electronic Structure and Oxygen Reduction Activity of SrTi 1- x Fe x O 3 Surfaces. Energy Environ. Sci. 2012, 5 (7), 7979–7988.

[16] Jung, W.; Tuller, H. L. Investigation of Surface Sr Segregation in Model Thin Film Solid Oxide Fuel Cell Perovskite Electrodes. Energy Environ. Sci. 2012, 5 (1), 5370–5378.

[17] Navickas, E.; Huber, T.; Chen, Y.; Hetaba, W.; Holzlechner, G.; Rupp, G.; Stöger-Pollach, M.; Friedbacher, G.; Hutter, H.; Yildiz, B.; Fleig, J. Fast Oxygen Exchange and Diffusion Kinetics of Grain Boundaries in Sr-Doped LaMnO3 Thin Films. Phys. Chem. Chem. Phys. 2015, 17 (12), 7659-7669.

[18] Chen, T.; Harrington, G. F.; Sasaki, K.; Perry, N. H. Impact of Microstructure and Crystallinity on Surface Exchange Kinetics of Strontium Titanium Iron Oxide Perovskite by In Situ Optical Transmission Relaxation Approach. J Mater Chem A 2017, 5, 23006-23019.

[19] Yan, L.; Kavaipatti, B.; Chang, K.; You, H.; Salvador, P. Microstructural Effects on the Oxygen Exchange Kinetics of La0.7Sr0.3MnO3 Thin Films. ECS Trans. 2011, 35 (1), 2063-2075.

[20] Kerman, K.; Ko, C.; Ramanathan, S. Orientation Dependent Oxygen Exchange Kinetics on Single Crystal SrTiO3 Surfaces. Phys. Chem. Chem. Phys. PCCP 2012, 14 (34), 11953–11960.

[21] Chen, T.; Harrington, G. F.; Masood, J.; Sasaki, K.; Perry, N. H. Emergence of Rapid Oxygen Surface Exchange Kinetics During In Situ Crystallization of Mixed Conducting Thin Film Oxides. ACS Appl. Mater. Interfaces 2019, 11 (9), 9102-9116.

[22] Perry, N. H.; Pergolesi, D.; Bishop, S. R.; Tuller, H. L. Defect Chemistry and Surface Oxygen Exchange Kinetics of La-Doped Sr(Ti,Fe)O3 - α in Oxygen-Rich Atmospheres. Solid State Ion. 2015, 273, 18–24.

[23] Yang, Y. L.; Chen, C. L.; Chen, S. Y.; Chu, C. W.; Jacobson, A. J. Impedance Studies of Oxygen Exchange on Dense Thin Film Electrodes of La0.5Sr0.5CoO3 − δ. J. Electrochem. Soc. 2000, 147 (11), 4001–4007.

[24] Perry, N. H.; Kim, J. J.; Tuller, H. L. Oxygen Surface Exchange Kinetics Measurement by Simultaneous Optical Transmission Relaxation and Impedance Spectroscopy: Sr(Ti,Fe)O 3-x Thin Film Case Study. Sci. Technol. Adv. Mater. 2018, 19, 130–141.

[25] Jung, W.; Tuller, H. L. Impedance Study of SrTi 1−xFe XO 3−δ (x = 0.05 to 0.80) Mixed Ionic-Electronic Conducting Model Cathode. Solid State Ion. 2009, 180, 843–847.

[26] Kim, J. J.; Bishop, S. R.; Thompson, N. J.; Tuller, H. L. Investigation of Redox Kinetics by Simultaneous In Situ Optical Absorption Relaxation and Electrode Impedance Measurements: Pr Doped Ceria Thin Films. Chem. Mater. 2014, 26 (3), 1374-1379.

[27] Ishigaki, T.; Yamauchi, S.; Kishio, K.; Mizusaki, J.; Fueki, K. Diffusion of Oxide Ion Vacancies in Perovskite-Type Oxides. J. Solid State Chem. 1988, 73 (1), 179–187.

[28] De Souza, R. A.; Kilner, J. A.; Walker, J. F. A SIMS Study of Oxygen Tracer Diffusion and Surface Exchange in La0.8Sr0.2MnO3+δ. Mater. Lett. 2000, 43 (1), 43–52.

[29] Yang, Q.; Burye, T. E.; Lunt, R. R.; Nicholas, J. D. In Situ Oxygen Surface Exchange Coefficient Measurements on Lanthanum Strontium Ferrite Thin Films via the Curvature Relaxation Method. Solid State Ion. 2013, 249–250, 123–128.

[30] Moreno, R.; García, P.; Zapata, J.; Roqueta, J.; Chaigneau, J.; Santiso, J. Chemical Strain Kinetics Induced by Oxygen Surface Exchange in Epitaxial Films Explored by Time-Resolved X-Ray Diffraction. Chem. Mater. 2013, 25 (18), 3640–3647.

[31] Haar, L. M. van der; Otter, M. W. den; Morskate, M.; Bouwmeester, H. J. M.; Verweij, H. Chemical Diffusion and Oxygen Surface Transfer of La1 − x Sr x CoO3 − δ Studied with Electrical Conductivity Relaxation. J. Electrochem. Soc. 2002, 149 (3), J41–J46.

[32] ten Elshof, J. E.; Lankhorst, M. H. R.; Bouwmeester, H. J. Oxygen Exchange and Diffusion Coefficients of Strontium-Doped Lanthanum Ferrites by Electrical Conductivity Relaxation. J. Electrochem. Soc. 1997, 144 (3), 1060–1067.

[33] Tsuchiya, M.; Bojarczuk, N. A.; Guha, S.; Ramanathan, S. Microstructural Effects on Electrical Conductivity Relaxation in Nanoscale Ceria Thin Films. J. Chem. Phys. 2009, 130 (17), 174711.

[34] Yasuda, I.; Hikita, T. Precise Determination of the Chemical Diffusion Coefficient of Calcium-Doped Lanthanum Chromites by Means of Electrical Conductivity Relaxation. J. Electrochem. Soc. 1994, 141 (5), 1268–1273.

[35] Bishop, S. R.; Druce, J.; Kim, J. J.; Kilner, J. A.; Tuller, H. L. Observation of Surface Impurities in Pr0.1Ce0.9O2- Thin Films Following Optical Absorption Relaxation Measurements. ECS Trans. 2013, 50 (27), 35–38.

[36] Zhao, L.; Perry, N. H.; Daio, T.; Sasaki, K.; Bishop, S. R. Improving the Si Impurity Tolerance of Pr0.1Ce0.9O2−δ SOFC Electrodes with Reactive Surface Additives. Chem. Mater. 2015, 27 (8), 3065–3070.

[37] De Souza, R. A.; Martin, M. Secondary Ion Mass Spectrometry (SIMS) – a Powerful Tool for Studying Mass Transport over Various Length Scales. Phys. Status Solidi C 2007, 4 (6), 1785–1801.

[38] Kilner, J.; Skinner, S.; Brongersma, H. The Isotope Exchange Depth Profiling (IEDP) Technique Using SIMS and LEIS. J. Solid State Electrochem. January 5, 15, 861–876.

[39] Lasia, A. Electrochemical Impedance Spectroscopy and Its Applications. In Modern Aspects of Electrochemistry; Conway, B. E., Bockris, J. O., White, R. E., Eds.; Modern Aspects of Electrochemistry; Springer US: Boston, MA, 2002; pp 143–248.

[40] Buckner, H.; Perry, N. H. In Situ Optical Absorption Studies of Point Defect Kinetics and Thermodynamics in Oxide Thin Films. Adv. Mater. Interfaces 2019, 6, 1900496.

[41] Kan, C. C.; Wachsman, E. D. Isotopic-Switching Analysis of Oxygen Reduction in Solid Oxide Fuel Cell Cathode Materials. Solid State Ion. 2010, 181, 338–347.

[42] Yasuda, I.; Hishinuma, M. Electrical Conductivity and Chemical Diffusion Coefficient of Strontium-Doped Lanthanum Manganites. J. Solid State Chem. 1996, 123 (2), 382–390.

[43] la O', G. J.; Shao-Horn, Y. Oxygen Surface Exchange Kinetics on Sr-Substituted Lanthanum Manganite and Ferrite Thin-Film Microelectrodes. J. Electrochem. Soc. 2009, 156 (7), B816.

[44] Fleig, J.; Kim, H. R.; Jamnik, J.; Maier, J. Oxygen Reduction Kinetics of Lanthanum Manganite (LSM) Model Cathodes: Partial Pressure Dependence and Rate-Limiting Steps. Fuel Cells 2008, 8, 330–337.

[45] Armstrong, E. N.; Duncan, K. L.; Wachsman, E. D. Effect of A and B-Site Cations on Surface Exchange Coefficient for ABO3 Perovskite Materials. Phys. Chem. Chem. Phys. 2013, 15 (7), 2298–2308.

[46] Ganeshananthan, R.; Virkar, A. V. Measurement of Surface Exchange Coefficient on Porous La0.6Sr0.4CoO3−δ Samples by Conductivity Relaxation. J. Electrochem. Soc. 2005, 152 (8), A1620.

[47] Wilson, J. R.; Kobsiriphat, W.; Mendoza, R.; Chen, H.-Y.; Hiller, J. M.; Miller, D. J.; Thornton, K.; Voorhees, P. W.; Adler, S. B.; Barnett, S. A. Three-Dimensional Reconstruction of a Solid-Oxide Fuel-Cell Anode. Nat. Mater. 2006, 5 (7), 541–544.

[48] Kim, J. J.; Bishop, S. R.; Chen, D.; Tuller, H. L. Defect Chemistry of Pr Doped Ceria Thin Films Investigated by in Situ Optical and Impedance Measurements. Chem. Mater. 2017, 29 (5), 1999–2007.

[49] Kim, J. J.; Bishop, S. R.; Thompson, N. J.; Chen, D.; Tuller, H. L. Investigation of Nonstoichiometry in Oxide Thin Films by Simultaneous in Situ Optical Absorption and Chemical Capacitance Measurements: Pr-Doped Ceria, a Case Study. Chem. Mater. 2014, 26 (3), 1374–1379.

[50] Rothschild, A.; Menesklou, W.; Tuller, H. L.; Ivers-Tiffée, E. Electronic Structure, Defect Chemistry, and Transport Properties of SrTi1-XFexO3-y Solid Solutions. Chem. Mater. 2006, 18 (16), 3651–3659.

[51] Perry, N. H.; Kim, N.; Ertekin, E.; Tuller, H. L. Origins and Control of Optical Absorption in a Nondilute Oxide Solid Solution: Sr(Ti,Fe)O3–x Perovskite Case Study. Chem. Mater. 2019, 31 (3), 1030–1041.

[52] Harrington, G. F.; Kalaev, D.; Yildiz, B.; Sasaki, K.; Perry, N. H.; Tuller, H. L. Tailoring Nonstoichiometry and Mixed Ionic Electronic Conductivity in Pr0.1Ce0.9O2−δ/SrTiO3 Heterostructures. ACS Appl. Mater. Interfaces 2019, 11 (38), 34841–34853.

[53] Luiskutty, C. T.; Ouseph, P. J. Valence States of Iron in Photochromic Strontium Titanate by Mössbauer Effect. Solid State Commun. 1973, 13 (3), 405–409.

[54] Merkle, R.; Maier, J. Oxygen Incorporation into Fe-Doped SrTiO3: Mechanistic Interpretation of the Surface Reaction. Phys. Chem. Chem. Phys. 2002, 4, 4140-4148.

[55] Kuhn, M.; Kim, J. J.; Bishop, S. R.; Tuller, H. L. Oxygen Nonstoichiometry and Defect Chemistry of Perovskite-Structured BaxSr1–XTi1–YFeyO3–y/2+δ Solid Solutions. Chem. Mater. 2013, 25, 2970–2975.

[56] Perry, N. H.; Kim, J. J.; Bishop, S. R.; Tuller, H. L. Strongly Coupled Thermal and Chemical Expansion in the Perovskite Oxide System Sr(Ti,Fe)O3−α. J. Mater. Chem. A 2015, 3 (7), 3602–3611.

[57] Jung, W.; Tuller, H. L. Investigation of Cathode Behavior of Model Thin-Film SrTi1- x Fe x O3- δ (X= 0.35 and 0.5) Mixed Ionic-Electronic Conducting Electrodes. J. Electrochem. Soc. 2008, 155 (11), B1194–B1201.

[58] Hsu, C. H.; Mansfeld, F. Technical Note: Concerning the Conversion of the Constant Phase Element Parameter Y0 into a Capacitance. CORROSION 2001, 57 (9), 747–748.

[59] Jung, W.; Tuller, H. L. A New Model Describing Solid Oxide Fuel Cell Cathode Kinetics: Model Thin Film SrTi1-XFexO3-δ Mixed Conducting Oxides–a Case Study. Adv. Energy Mater. 2011, 1 (6), 1184–1191.

[60] Merkle, R.; De Souza, R. A.; Maier, J. Optically Tuning the Rate of Stoichiometry Changes: Surface-Controlled Oxygen Incorporation into Oxides under UV Irradiation. Angew. Chem. Int. Ed Engl. 2001, 40 (11), 2126–2129.

[61] Dietz, G. W.; Antpöhler, W.; Klee, M.; Waser, R. Electrode Influence on the Charge Transport through SrTiO3 Thin Films. J. Appl. Phys. 1995, 78 (10), 6113–6121.

[62] Dietz, G. W.; Schumacher, M.; Waser, R.; Streiffer, S. K.; Basceri, C.; Kingon, A. I. Leakage Currents in Ba0.7Sr0.3TiO3 Thin Films for Ultrahigh-Density Dynamic Random Access Memories. J. Appl. Phys. 1997, 82 (5), 2359–2364.

[63] Fujimaki, Y.; Nakamura, T.; Develos-Bagarinao, K.; Yamaji, K.; Yashiro, K.; Kawada, T.; Iguchi, F.; Yugami, H.; Amezawa, K. Quantitative Evaluation of Electrochemically Active Area in an SOFC Cathode by Oxygen Isotopic Exchange Measurements of a Model Patterned Electrode. ECS Trans. 2015, 68 (1), 623.

[64] Amezawa, K.; Fujimaki, Y.; Mizuno, K.; Kimura, Y.; Nakamura, T.; Nitta, K.; Terada, Y.; Iguchi, F.; Yugami, H.; Yashiro, K.; Kawada, T. (Invited) Triple Phase Boundary Reaction in a Mixed-Conducting SOFC Cathode. ECS Trans. 2017, 77 (10), 41.

[65] Baker, R.; Guindet, J.; Kleitz, M. Classification Criteria for Solid Oxide Fuel Cell Electrode Materials. J. Electrochem. Soc. 1997, 144 (7), 2427.

[66] Leonhardt, M.; De Souza, R. A.; Claus, J.; Maier, J. Surface Kinetics of Oxygen Incorporation into SrTiO3. J. Electrochem. Soc. 2002, 149 (2), J19.

[67] Su, R.; Lü, Z.; Jiang, S. P.; Shen, Y.; Su, W.; Chen, K. Ag Decorated (Ba,Sr)(Co,Fe)O3 Cathodes for Solid Oxide Fuel Cells Prepared by Electroless Silver Deposition. Int. J. Hydrog. Energy 2013, 38 (5), 2413–2420.

[68] Liu, Y.; Hashimoto, S.; Yasumoto, K.; Takei, K.; Mori, M.; Funahashi, Y.; Fijishiro, Y.; Hirano, A.; Takeda, Y. Preparation and Application of Nano-Dispersed Ag in La0.6Sr0.4CoxFe1−xO3−δ Perovskites for Intermediate-Temperature Solid Oxide Fuel Cell. Curr. Appl. Phys. 2009, 9 (1, Supplement), S51–S53.

[69] Guo, Y.; Zhou, Y.; Chen, D.; Shi, H.; Ran, R.; Shao, Z. Significant Impact of the Current Collection Material and Method on the Performance of Ba0.5Sr0.5Co0.8Fe0.2O3−δ Electrodes in Solid Oxide Fuel Cells. J. Power Sources 2011, 196 (13), 5511–5519.

Table of Contents Graphic

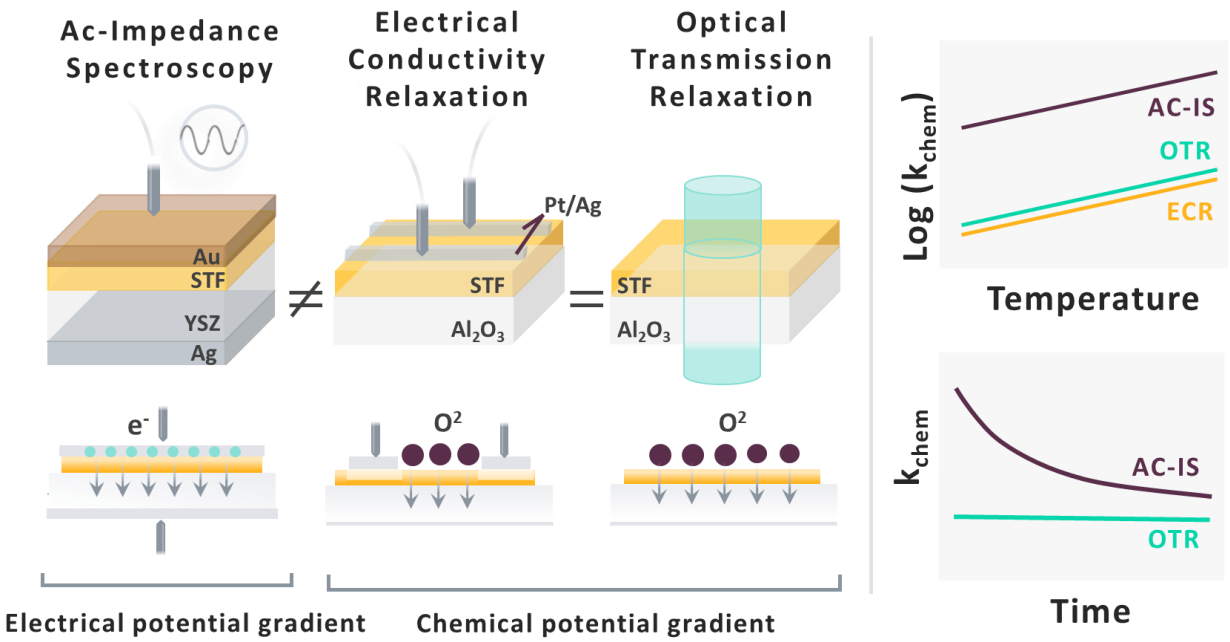

Supporting Information

Simultaneous Electrical, Electrochemical, and Optical Relaxation Measurements of Oxygen Surface Exchange Coefficients: $Sr(Ti,Fe)O_{3-d}$ Film Crystallization Case Study

Emily J. Skiba[1,§], Ting Chen[2,Δ,§], and Nicola H. Perry[1,2]*

[1] Department of Materials Science & Engineering and Materials Research Laboratory, University of Illinois at Urbana-Champaign, 1304 W Green St, Urbana IL 61801, U.S.A.

[2] International Institute for Carbon-Neutral Energy Research, Kyushu University, 744 Motooka, Nishi-ku Fukuoka, 819-0395 Japan

[Δ] Present affiliation: Toyota Motor Engineering & Manufacturing (China) Co., Ltd, Dongsihuang Road No.55, Changshu, Jiangsu, China

[§] These authors contributed equally

* Corresponding author email: nhperry@illinois.edu

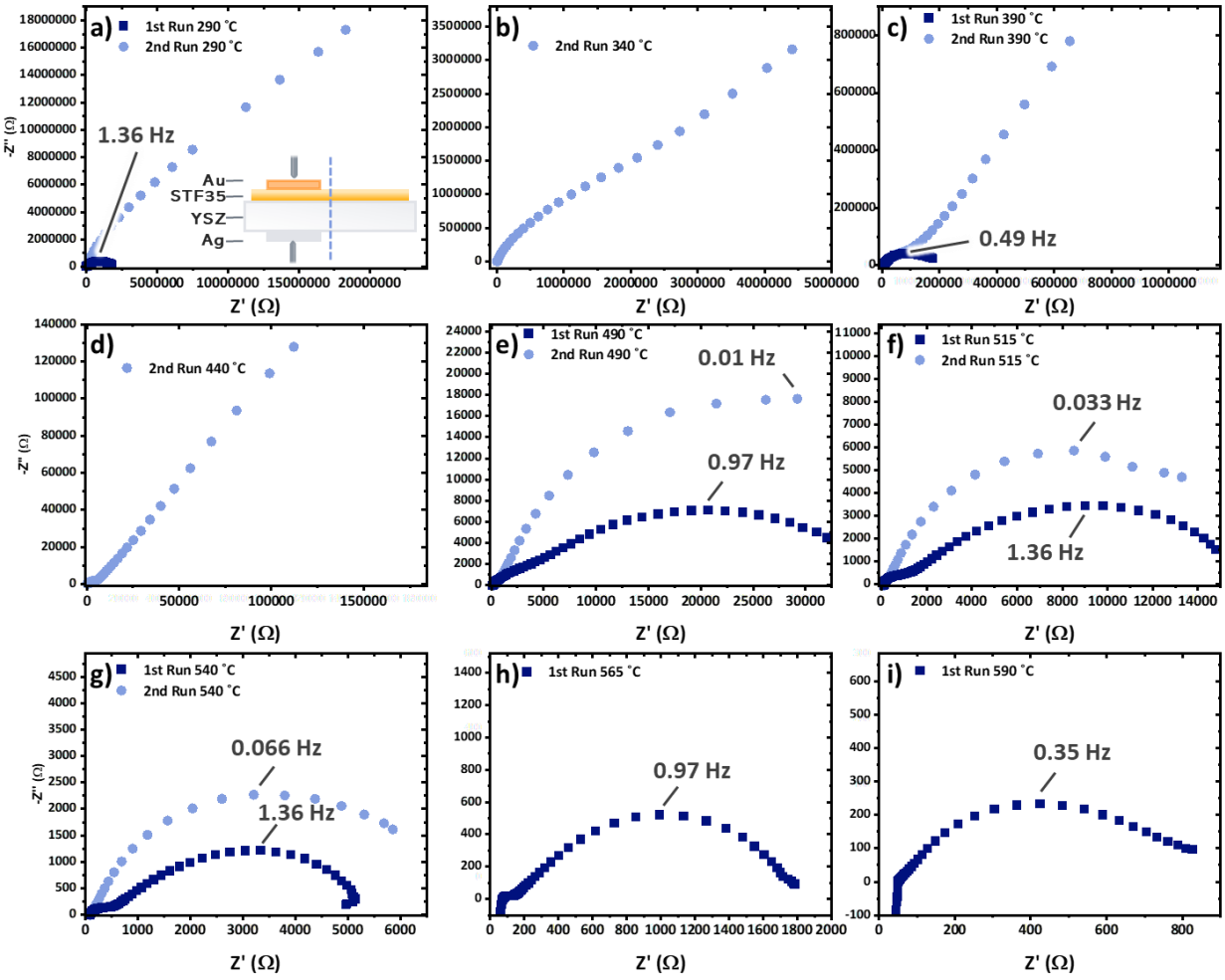

Figure S1. Nyquist plots from cross-cell impedance data of 25 ˚C-grown film from first (dark blue squares) and second measurement cycles (light blue circles), taken as a function of temperature: a) 290˚C, b) 340 ˚C, c) 390 ˚C, d) 440 ˚C, e) 490 ˚C, f) 515 ˚C, g) 540 ˚C, h) 565 ˚C, i)590 ˚C. Inset of first graph shows the asymmetric cell configuration used for these measurements. Spectra consist of several arcs, with the low frequency arc corresponding to the oxygen surface exchange response of the film/current collector.

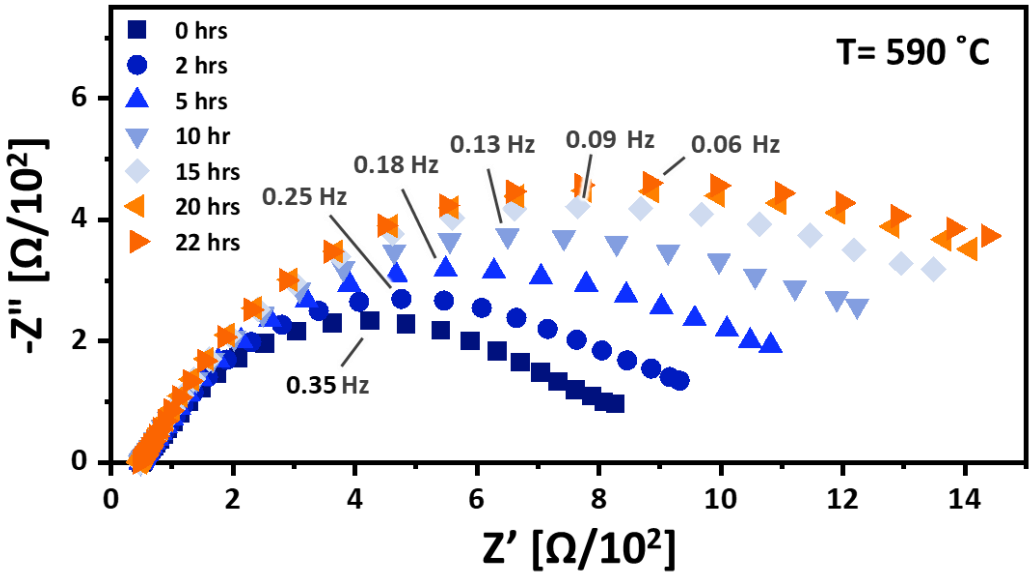

Figure S2. Nyquist plots from cross-cell impedance data of 25 ˚C-grown film following crystallization. Aging study to confirm the degradation of apparent AC-IS k_{chem} relative to OTR k_{chem} values was conducted for 22 hours at 590 ˚C. Increase in low frequency arc time constant corresponds to a decrease in k_{chem}.

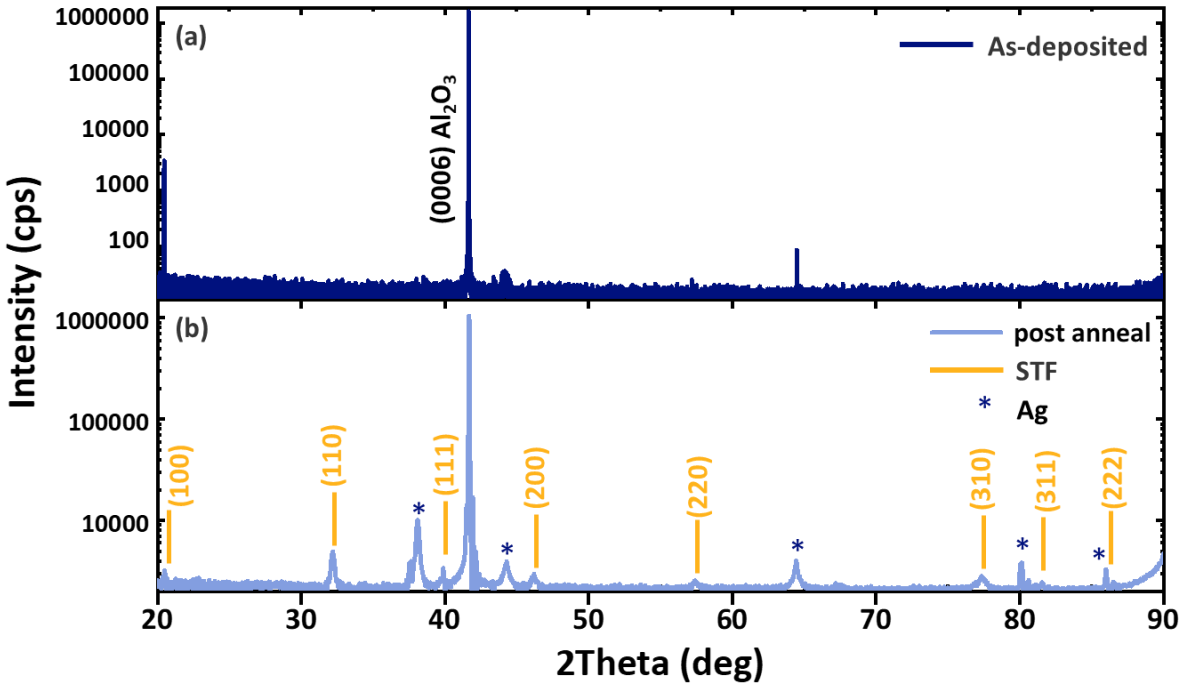

Figure S3. XRD patterns of 400 °C-grown film on (0001) Al_2O_3 a) prior to and b) following second measurement cycles. Peaks attributed to silver are due to the presence of the Ag current collectors on the surface of the film.

Table S1. Fitted k_{chem} for 25 ˚C-grown film from oxidation (final pO_2 = 0.21 atm) and reduction relaxations (final pO_2 = 0.04 atm) for OTR/AC-IS techniques during the first measurement run.

Temp. (˚C)	*OTR k_{chem} (cm/s)* *pO_2= 0.04 atm*	*OTR k_{chem} (cm/s)* *pO_2= 0.21 atm*	*AC-IS k_{chem} (cm/s)* *pO_2 = 0.21 atm*
488	--	--	2.64 x10^{-5}
513	1.80 x10^{-6}	2.00 x10^{-6}	3.31 x10^{-5}
540	1.34 x10^{-6}	2.14 x10^{-6}	4.03 x10^{-5}
565	--	--	3.97 x10^{-5}
590	1.95 x10^{-6}	2.45 x10^{-6}	1.82 x10^{-5}

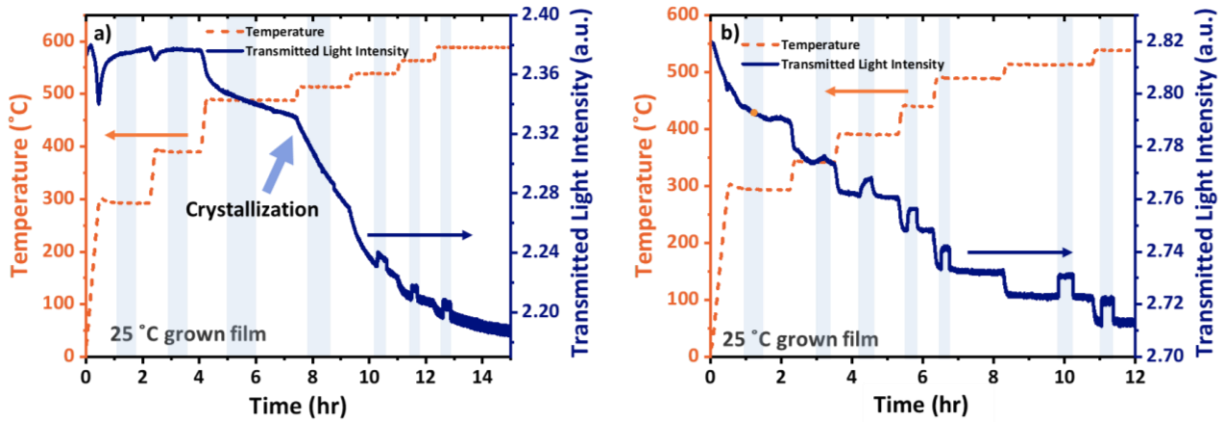

Figure S4. a), b) Transmitted light intensity, pO_2, and temperature as a function of time for 1st and 2nd measurement of oxygen reduction/oxidation relaxation of 25 ˚C, amorphous as-deposited film. Shaded regions correspond to a pO_2 of 0.04 atm and white regions to a pO_2 of 0.21 atm.

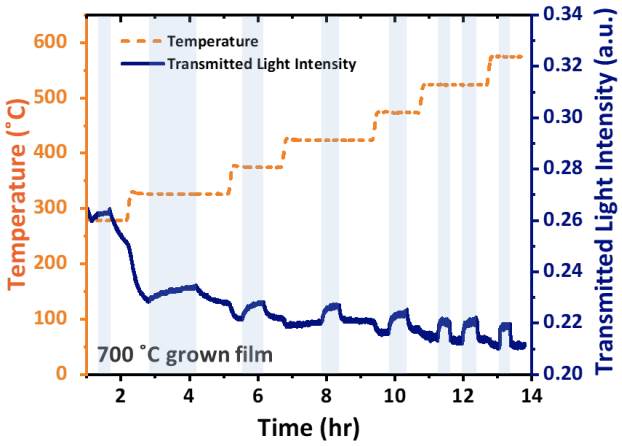

Figure S5. Transmitted light intensity, pO_2, and temperature as a function of time for 1st measurement of oxygen reduction/oxidation relaxation of crystalline as-deposited, 700 ˚C-grown film. Shaded and unshaded regions correspond to a pO_2 of 0.04 atm and 0.21 atm, respectively.

Table S2. Fitted k_{chem} for 700 ˚C-grown film from oxidation (final pO_2 = 0.21 atm) and reduction relaxations (final pO_2 = 0.04 atm) for OTR/ECR techniques during the first measurement run.

Temp. (˚C)	*ECR k_{chem} (cm/s), pO2 = 0.04 atm*	*OTR k_{chem} (cm/s), pO2 = 0.04 atm*	*ECR k_{chem} (cm/s), pO2 = 0.21 atm*	*OTR k_{chem} (cm/s), pO2 = 0.21 atm*
325	7.70×10^{-9}	1.02×10^{-8}	1.21×10^{-8}	1.07×10^{-8}
375	2.78×10^{-8}	1.87×10^{-8}	--	2.28×10^{-8}
425	--	3.39×10^{-8}	--	4.63×10^{-8}
475	--	4.56×10^{-8}	5.37×10^{-8}	5.22×10^{-8}
525	--	1.07×10^{-7}	1.13×10^{-7}	1.58×10^{-7}
575	2.55×10^{-7}	2.23×10^{-7}	2.32×10^{-7}	1.63×10^{-7}

Table S3. Fitted k_{chem} for 400 ˚C-grown film from oxidation (final pO_2 = 0.21 atm) and reduction relaxations (final pO_2 = 0.04 atm) for OTR/ECR techniques during the second measurement run.

Temp. (˚C)	*ECR k_{chem} (cm/s), pO2 = 0.04 atm*	*OTR k_{chem} (cm/s), pO2 = 0.04 atm*	*ECR k_{chem} (cm/s), pO2 = 0.21 atm*	*OTR k_{chem} (cm/s), pO2 = 0.21 atm*
333	4.58×10^{-8}	5.31×10^{-8}	7.01×10^{-8}	1.03×10^{-7}
382	3.32×10^{-7}	2.85×10^{-7}	5.48×10^{-7}	8.08×10^{-7}
431	1.48×10^{-6}	1.42×10^{-6}	2.22×10^{-6}	1.72×10^{-6}
482	2.56×10^{-6}	2.08×10^{-6}	3.10×10^{-6}	2.36×10^{-6}
533	2.73×10^{-6}	2.17×10^{-6}	2.86×10^{-6}	1.68×10^{-6}

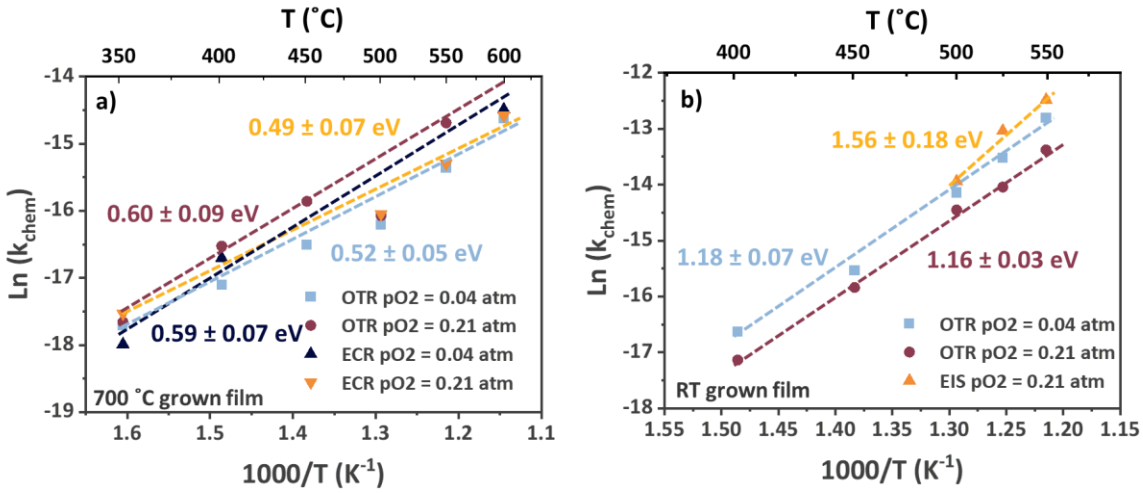

Figure S6. a), b) show the activation energy from fitted k_{chem} values for the 700 ˚C- and 25 ˚C-grown films, respectively.